Synthetic Aperture Imaging in the Optical Domain

Yap Jun Yan

Advisor: Christian Kurtsiefer

Department of Physics, Faculty of Science
National University of Singapore

This thesis is submitted for the degree of
Bachelor of Science (Honours)

April 2021

Acknowledgements

First, I would like to thank Professor Christian for offering me the opportunity to work on this project, as well as the encouragement and guidance throughout this short but fruitful year.

Next, I would like to thank Peng Kian, for your supervision and guidance over the course of the project. You have definitely taught me important lessons, both in physics and in life. Thank you for your patience, especially so when I am stubborn and tend to give up easily. Despite the ups and downs, I am still grateful for helping me improve as a person.

To everyone else in the Quantum Optics group, thank you for the warmth and kindness, especially when I needed to find stuff or equipment in the lab. You guys made FYP a pleasant and inclusive experience despite the COVID-19 pandemic.

Finally, to my friends and family. Thank you for being the pillar of support throughout this relatively tough period of my undergraduate life. Honestly, I would likely have given up if it was not for the encouragement and optimism you guys gave.

Abstract

The wave-like properties of photons gives rise to diffraction, or the bending of waves when passing through an object or an aperture. Diffraction limits the resolution of an aperture, with larger apertures being able to resolve smaller objects. This project aims to use intensity correlation of photons to resolve objects that would otherwise be unresolvable according to Rayleigh's Criterion. The temporal and spatial domain of intensity correlations provides information on the light source's spectral distribution and spatial intensity distribution. We recreate a bunched light source in the lab with a semiconductor laser diode below threshold, or the point where a laser diode transits to be a coherent light source. A temporal normalised intensity correlation of 1.63 was obtained. Whilst spatial domain information was not obtained, we list the problems and challenges faced during the setup process for future research considerations.

Table of contents

List of Figures

List of Tables

Nomenclature

Other Symbols

b	Baseline Separation between 2 Detectors
J_1	First Order Bessel Function of the First Kind
FSR	Free Spectral Range
$\mathcal{F}$	Fourier Transform
FWHM	Full-Width at Half-Maximum
$^{\lambda}/_{2}$	Half-Wave plate
HBT	Hanbury-Brown Twiss
λ	Wavelength in medium
LED	Light-Emitting Diode
$\Delta\omega$	Spectral Linewidth
mas	Milli-Arcsecond
ν	Frequency
n	Refractive Index
SNR	Signal-To-Noise Ratio
τ	Timing separation between photoevents
τ_c	Coherence Time

Acronyms / Abbreviations

APD	Avalanche Photodiode
BS	Beam-Splitter
CL	Collimating Lens
LD	Laser Diode
LP	Linear Polariser
MMF	Multi Mode Fibre
NPBS	Non-Polarising Beam-Splitter
PBS	Polarising Beam-Splitter
PC	Physical Contact
SMF	Single Mode Fibre

Chapter 1

Introduction

Print out a piece of paper with a letter 'O' in the middle. Place it a metre away, you will still be able to make out the shape of the letter. Place it a kilometre away, are you still able to tell if it is a letter 'O'? Probably not. The resolution limit of our eyes is about half a degree, or 0.5 arcminutes. That means that for the human eye to be able to distinguish the letter 'O' at a kilometre away, the letter has to be at least 8.7-metres wide. This is known as the resolution limit of the optical system, in this case – the resolution limit of the human eye.

When light passes through an aperture, it gets diffracted and the image formed has a characteristic pattern depending on the shape of the aperture. For a circular aperture like for the human eye, the image has an airy disk pattern. Different points of the source form different images, and the point where the images cannot be differentiated from one another is known as the resolution limit. The resolution limit of optical systems is commonly described by the Rayleigh's Criterion [1]:

$$\theta = \frac{1.22\lambda}{b}, \tag{1.1}$$

where θ refers to the angular resolution, λ the wavelength of light involved and b the aperture size of the optical system.

A graphical representation of equation (1.1) is shown below:

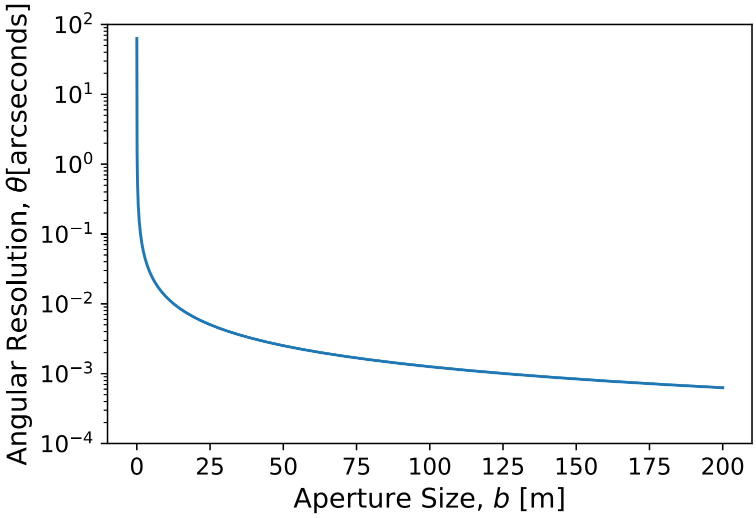

Fig. 1.1 Angular resolution θ of an optical system with varying b from 0 m to 200 m. Plot shown is for $\lambda = 500\,\mathrm{nm}$

In order for better resolution, such as sub-milliarcsecond (mas) angular resolution, aperture sizes greater than 125 m is required. Single mirror and lens with sizes of this magnitude are impractical given the cost and mechanical equipment required to keep them stable. Instead, we can use interferometry techniques. Interferometry works on the coherence property of light in time and space.

1.1 Coherence of Light

1.1.1 First Order Correlation Function, $g^{(1)}$

One such interferometry technique is the Michelson interferometry, which examines the correlation of light fields. The correlation of light fields is given by the first order correlation function $g^{(1)}$. It is defined as:

$$g^{(1)}(\tau, r_1, r_2) = \frac{\langle \epsilon^*(t, r_1)\epsilon(t+\tau, r_2)\rangle}{\sqrt{\langle |\epsilon(t, r_1)|^2\rangle \langle |\epsilon(t+\tau, r_2)|^2\rangle}}, \tag{1.2}$$

with the $\langle ... \rangle$ representing the statistical average over a long time interval, $\epsilon(t, r_1, r_2)$ being the electric field of the light beam, τ the timing separation between the detected light fields and r_1 and r_2 the position transverse to the direction of propogation of the light field.

For zero spatial separation (ie. $r_1 = r_2$), also known as the autocorrelation of the electric field, by the Wiener-Khintchine Theorem [2, 3], the Fourier transform gives us the spectral distribution $S(\nu)$ of the light source:

$$S(\nu) \propto \mathcal{F}\{g^{(1)}(\tau, r_1 = r_2)\}, \tag{1.3}$$

where $\mathcal{F}$ is the Fourier transform.

For zero timing separation between the light fields (ie. $\tau = 0$), , the spatial first order correlation function γ_{12} gives:

$$\gamma_{12} = \frac{\langle \epsilon^*(t, r_1)\epsilon(t, r_2)\rangle}{\sqrt{\langle|\epsilon(t, r_1)|^2\rangle \langle|\epsilon(t, r_2)|^2\rangle}}, \tag{1.4}$$

For a light source with angular distance much smaller than the distance between the source and detection plane, van-Cittert Zernike Theorem [4, 5] states that the spatial first order correlation function γ_{12} is proportional to the Fourier transform of the spatial intensity distribution of the source $S(u, v)$. In particular, for a spatially incoherent, uniform intensity, circular, quasi-monochromatic light source, the Fourier transform of the spatial intensity distribution is given as:

$$S(u, v) = \mathcal{F}\left\{\frac{2J_1(\pi\theta_{UD}b/\lambda_0)}{\pi\theta_{UD}b/\lambda_0}\right\}, \tag{1.5}$$

where J_1 is the first order Bessel function of the first kind, θ_{UD} the angular diameter of the source, $b = |r_1 - r_2|$ the baseline, (u, v) the coordinates in Fourier space and λ_0 the wavelength of light involved.

By obtaining both spectral distribution and spatial intensity distribution of the light source, a $g^{(1)}$ interferometer can reconstruct the image of the light source.

The spatial intensity distribution of the light source is measured by the fringe visibility. The fringe visibility V, of an interferometer is defined as:

$$V = \frac{I_{max} - I_{min}}{I_{max} + I_{min}} = |\gamma_{12}|, \tag{1.6}$$

where I_{max} and I_{min} refers to the maxima and minima of the interference fringes respectively. The fringe visibility is equal to the modulus of the spatial first order correlation function. When I_{min} = 0, the visibility is highest at 1, while visibility is minimum at 0 for $I_{max} = I_{min}$.

However, since first order correlation function refers to the correlation of light fields, stabilisation of phase fluctuations to the order of photon wavelengths is required.

Consider a quasi-monochromatic field $\epsilon(t)$ with a centre frequency ω_0 that varies with time such that

$$\epsilon(t) = \epsilon_0 e^{-i\omega_0 t} e^{i\phi(t)}, \tag{1.7}$$

with $\phi(t)$ being the time varying phase information. Substituting this equation to (1.2), we obtain

$$g^{(1)}(\tau) = e^{-i\omega_0 \tau} \left\langle e^{i[\phi(t+\tau) - \phi(t))]} \right\rangle, \tag{1.8}$$

From this, we can see that the factor of $\left\langle e^{i[\phi(t+\tau)-\phi(t))]} \right\rangle$, which averages to 0 if the timing separation τ is much larger than the coherence time, since $\phi(t+\tau)$ will be increasingly uncorrelated to $\phi(t)$ as τ increases. Similarly, for $\tau << \tau_c$, the $\left\langle e^{i[\phi(t+\tau)-\phi(t))]} \right\rangle$ term averages to 1. Since there is a dependence on the $\phi(t)$ term, phase shifts in the order of wavelengths can change the visibility.

Instead of the need to stabilise the optics to sub-wavelength precision or extra compensation to offset atmosphere seeing effects [6], we consider using intensity interferometry, or the second order correlation, which is the correlation of light intensities.

1.1.2 Second Order Correlation Function, $g^{(2)}$

The second order correlation, also known historically as the Hanbury-Brown Twiss (HBT) effect, is the correlation of intensities at two detectors observing the same light source. This correlation of intensities was first introduced March of 1954 [7] and later used to measure the angular diameters of thirty-two stars [8] with the Narrabri Stellar Intensity Interferometer (NSII). Using telescopes in the form of detectors spaced at distances up to 188 m apart, the NSII was able to resolve stars of angular resolutions in the order of 0.1 mas (about 1/3600000 of a degree). Its resolving power back in 1974 exceeds that of the largest single aperture optical telescope in the world today, the Gran Telescopio in Canarias, with a combined aperture size of 10.4 m and able to resolve just about 10 mas for visible wavelengths.

The relation between aperture size and angular resolution is again described by Rayleigh's Criterion in equation (1.1). With increasing aperture size, both real and synthetic (in the form of multiple telescopes spaced apart), objects that span a small angular separation can be resolved. The NSII is an example of a synthetic aperture interferometer with two telescopes spaced up to 188 m apart.

The second order correlation function $g^{(2)}(b,\tau)$ is defined as:

$$g^{(2)}(b,\tau) = \frac{\langle I(t) \cdot I(b,t+\tau)\rangle}{\langle I(t)\rangle \langle I(b,t+\tau)\rangle},$$

where t is the time at which a photoevent is detected and recorded, b the baseline and τ the timing separation between each photoevent. A drawing of a common setup used to measure the second order correlation function is shown in **Fig.**1.2.

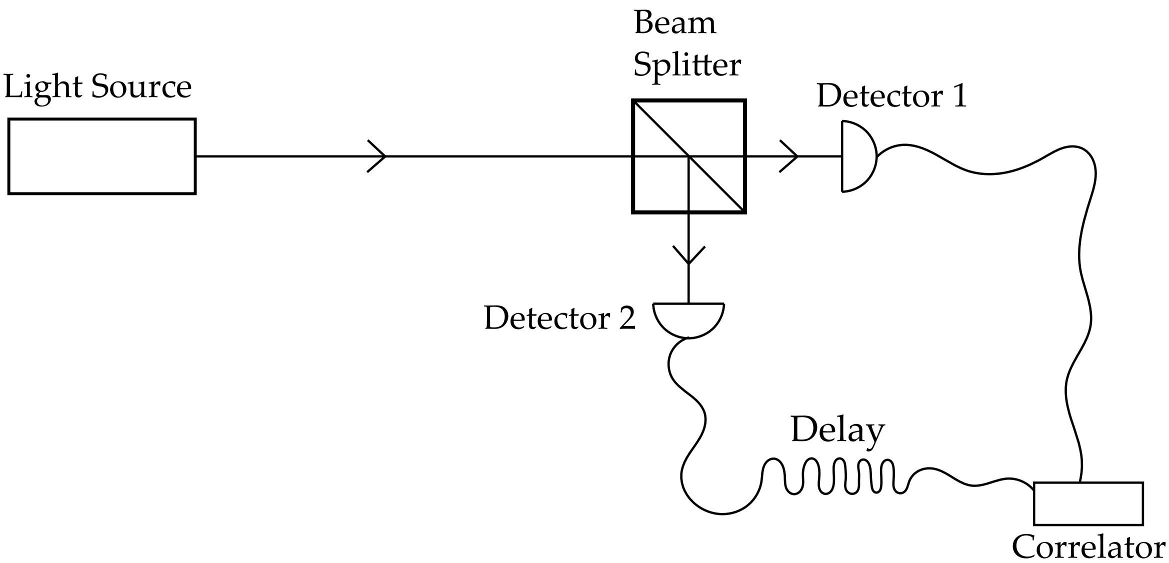

Fig. 1.2 Setup for measurement of temporal ($b = 0$) second order correlation. Light is incident on a beam splitter, which directs light into two separate detectors. The need for at least two detectors is to compensate for the dead time of the other detector. One of the detectors has an additional electronic delay to compensate for the dead time of the correlator such as a timestamp unit.

Since intensity is directly proportional to the photoevents, we can rewrite the temporal second order correlation function as

$$g^{(2)}(\tau) = \frac{\langle n_1(t) \cdot n_2(t+\tau) \rangle}{\langle n_1(t) \rangle \langle n_2(t) \rangle}$$

where $\langle ... \rangle$ represents the average over a time interval, n_1 and n_2 the number of photoevents detected at detectors 1 and 2 respectively (as shown in **Fig.** 1.2). $g^{(2)}(\tau)$ can be thought of as the ratio of coincident photoevents at separate detectors 1 and 2 over the product of independent/single photoevents at each detector. When describing this ratio of correlation between photons, the correlation is present for coherence time τ_c.

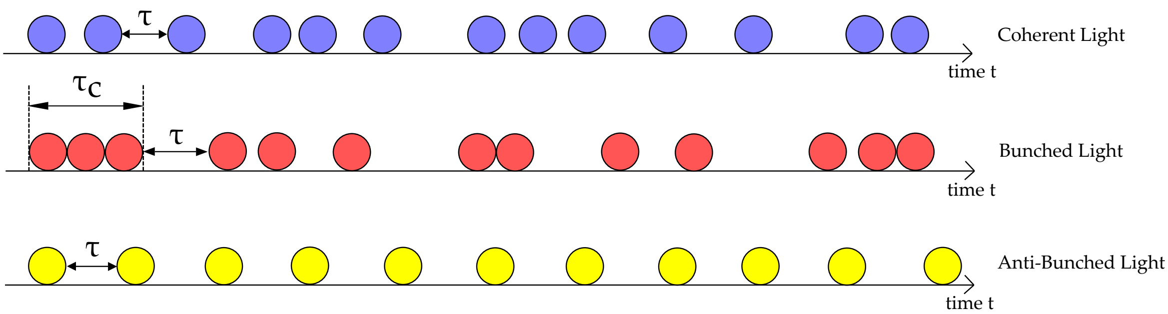

Fig. 1.3 Photon behaviour for bunched, coherent and anti-bunched light. It represents a snapshot in time where photons are propagating to the right. τ corresponds to the temporal separation between the photons, while τ_c corresponds to the time for which photons are correlated.

With reference to **Fig.** 1.3, for bunched light, such as chaotic light or thermal light, photons tend to travel in a bunch for short timescales (in the order of *ps* for blackbody radiation) corresponding to the coherence time. Chaotic light is radiation as a result of randomness of the excitation and phase interruption process in atomic collisions, such as atomic collisions in blackbody radiation.

For coherent light, such as laser light, photons arrive at the detector at random time intervals. There is a third kind of light, known as anti-bunched light. Photons tend to prefer to space out as evenly as possible. An example of such a light source is light from quantum dot device.

Within this timescale τ_c, coherence between light beams is present when the superposition of these light beams results in a spatially fixed interference pattern [9]. The probability of coincident photoevents is greater than the expected for random photoevents, leading to a $g^{(2)}(\tau < \tau_c) > 1$. At timescales longer than the coherence time, superposition of light beams do not have a fixed interference at the plane of detection, leading to $g^{(2)}(\tau > \tau_c) = 1$.

For chaotic light with a lorentzian spectral linewidth, the second order correlation function is given by [10]:

$$g^{(2)}(\tau) = 1 + e^{-\frac{2|\tau|}{\tau_c}}, \tag{1.9}$$

which is the Fourier transform of a Lorentzian spectral distribution. Note that $g^{(2)}(\tau = 0)$ returns a value of 2 and decays to 1 as $\tau >> \tau_c$.

For coherent light, there is no correlation between photoevents and $g^{(2)}(\tau) = 1$ for all τ. For anti-bunched light, there is anti-correlation between photoevents and $g^{(2)}(\tau = 0) \longrightarrow 0$.

A plot that summarizes the second order temporal correlation function $g^{(2)}(\tau)$ for bunched and coherent and light is shown in **Fig.** 1.4. The plot for bunched light assumes a lorentzian spectral linewidth.

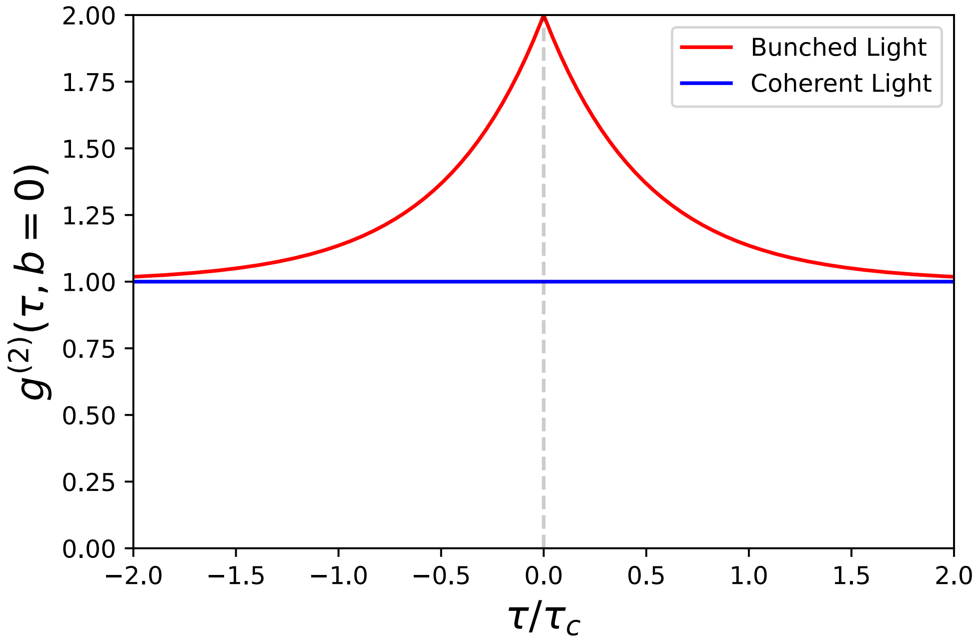

Fig. 1.4 $g^{(2)}(\tau)$ values for bunched and coherent light. The value of $g^{(2)}(\tau = 0)$ is 2 for bunched light and $g^{(2)}(\tau)$ is 1 throughout for coherent light.

For chaotic light (also known as thermal light), the second order correlation function $g^{(2)}(b,\tau)$ is related to the first order correlation function $g^{(1)}(b,\tau)$ in the Siegert relation [11]:

$$g^{(2)}(b,\tau) = 1 + \left|g^{(1)}(b,\tau)\right|^2, \tag{1.10}$$

which removes the phase information $\phi(t)$ through the modulus. However, the limitations include the need for a chaotic light source, as well as poor signal-to-noise ratio (SNR).

By incorporating the Siegert relation (1.10) with van-Cittert Zernike theorem (1.5), we obtain the following relation:

$$g^{(2)}(b,\tau=0) = 1 + \left|\frac{2J_1(\pi\theta_{UD}b/\lambda_0)}{\pi\theta_{UD}b/\lambda_0}\right|^2. \tag{1.11}$$

Equation (1.11) can be graphically plotted as such:

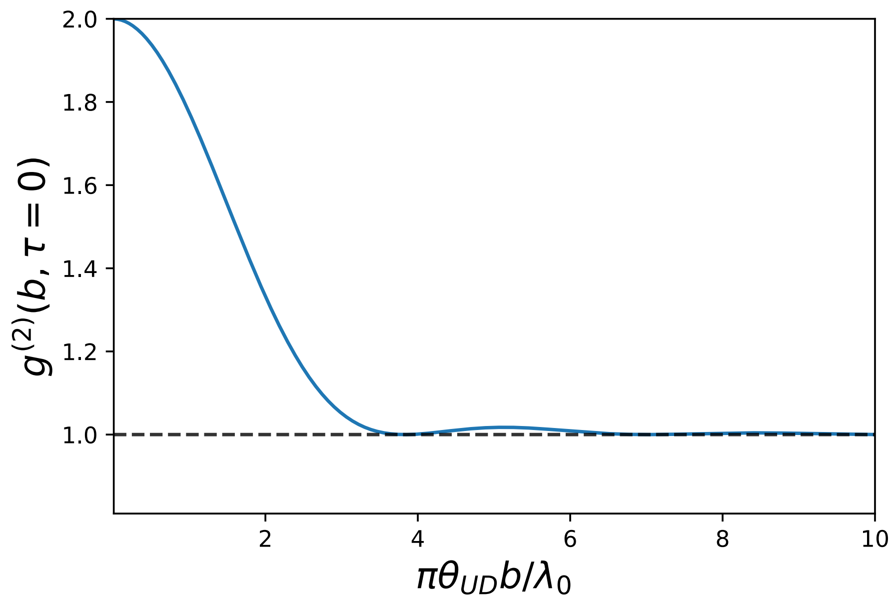

Fig. 1.5 Theoretical plot of spatial second order correlation $g^{(2)}(b,\tau=0)$ against baseline b for a uniform intensity, circular, quasi-monochromatic light source. First minima corresponds to a value of about 3.83.

With reference to **Fig.**1.5, the spatial second order correlation $g^{(2)}(b,\tau=0)$ decreases with increasing b, or decreasing correlation in space as the detectors move further apart, assuming other factors θ_{UD} and λ_0 are constant. From the same figure, the theoretical plot intersects with the horizontal axis at a value of 3.83. If we were to equate the intersection point as such

$$\frac{\pi\theta_{UD}b}{\lambda_0} = 3.83, \tag{1.12}$$

we then arrive at

$$\theta_{UD} = \frac{1.22\lambda_0}{b}, \tag{1.13}$$

which is Rayleigh's Criterion. By using the relation in equation (1.11), varying b allows us to obtain the spatial distribution of the light source. The first minima of a measurement in $g^{(2)}(b, \tau = 0)$ tells us the angular diameter of the light source.

While the NSII was able to measure the angular diameter of stars, it was unable to determine the spectral properties of stars, which can be obtained from the temporal second order correlation. A major limitation back then was the timing inefficiencies of detectors, with low quantum efficiencies and long dead time.

With advances in detectors having higher quantum efficiencies and shorter dead times, hopes of obtaining information on spectral distribution is possible. In 2014, the temporal correlation of intensities from our very own star, the Sun, was measured [12]. It was the first temporal correlation measurement of a blackbody. Temporal correlation of intensities of pseudothermal light sources have also been measured. Examples of pseudothermal light sources include laser scattering off a rotating ground glass [13], which introduces phase randomisation dependening on the frequency of rotation, as well as laser dispersing through a cloud of microspheres a few μm wide [14], which also causes phase randomisation of light passing through microspheres undergoing Brownian motion.

In this project, we aim to create a lab based setup to image a chaotic/thermal source. By obtaining both the temporal and spatial correlation of intensities of the source, we can then obtain the spatial intensity distribution along with the spectral distribution distribution. Accomplishing this indicates the potential of intensity interferometry for astronomy purposes in the visible spectrum of light.

1.2 Light Source

First, we aim to recreate a light source that has bunching in the lab with for intensity interferometry. Some of the options include using a Mercury low pressure vapour tube, a light-emitting diode (LED) as well as blackbody sources such as the Sun. However, due to the low power spectral density of sources such as a Mercury low pressure vapour tube, we look for other sources with a high power spectral density. Lasers came to mind as they have high power and narrow linewidths. However, a laser is a source of coherent light, which does not exhibit bunching. But, if the input current to the laser diode is sufficiently low, the laser diode can behave as a light-emitting diode, which is a source of bunched light.

Therefore, in the subsequent sections, we use a visible wavelength (rated at 515nm), gallium nitride (GaN) semiconductor laser diode (model L515A1 from Thorlabs) and run it at sufficiently low current levels.

There are two main regions that a semiconductor laser diode can operate in, one being a region of spontaneous emission and the other being simulated emission. The point at which this transition occurs is also known as the lasing threshold.

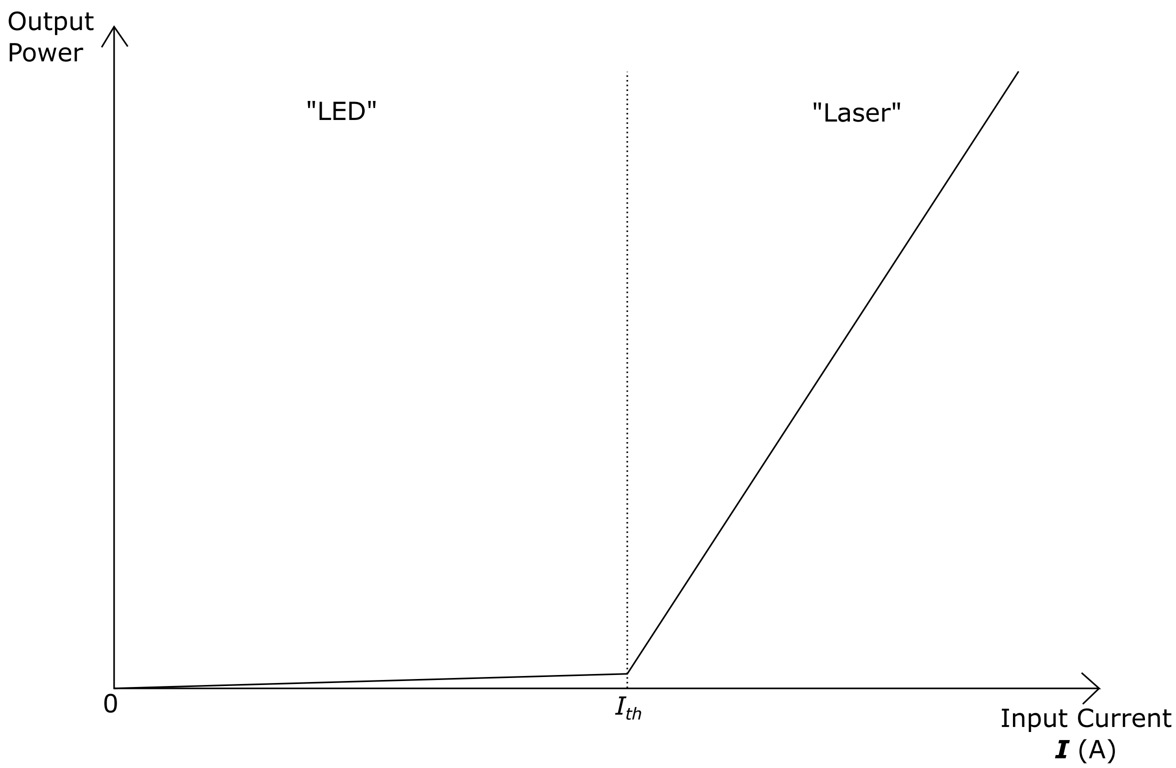

Fig. 1.6 Typical shape of a Power-Current curve of a laser diode

In the region below lasing threshold I_{th}, spontaneous emission, or photons released as a result of transition of atoms from a higher energy level to a lower energy level. Spontaneous emission results in photons released in random directions, in an incoherent manner. Light from semiconductor laser diode in this region behaves like a LED, or bunched light.

Above the lasing threshold, additional energy from increasing input current to the laser diode is passed into the coherently oscillating cavity mode. Photons released as simulated emission exit the cavity in the semiconductor laser diode and behaves like a laser.

1.2.1 Power-Current Curve

In order to create the bunched light source, we need to determine where the threshold lies and to run the semiconductor laser diode below the threshold. One way to determine this region would be to measure the output power P as a function of the input current I of the semiconductor laser diode.

Output power is measured through the use of a Silicon photodiode (model Hamamatsu S5107) that generates a photocurrent I_{PD}, which is converted to incident power through

$$P = \frac{I_{PD}}{R} \tag{1.14}$$

where R is the responsitivity of the photodiode at a certain wavelength.

A schematic setup for power-current measurements is shown below:

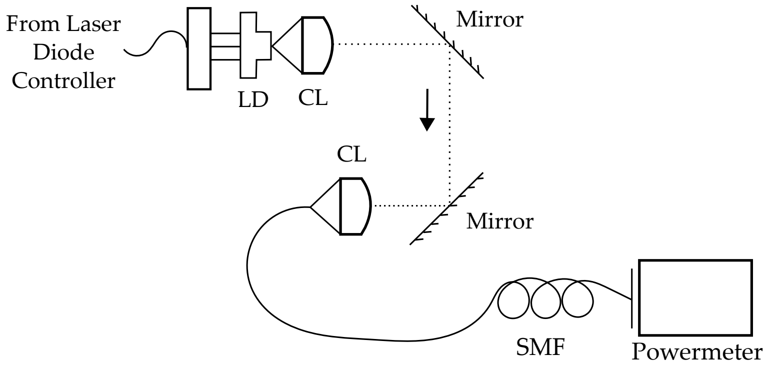

Fig. 1.7 The semiconductor laser diode (LD) is connected to a laser diode controller that varies the LD input current and the voltage across a peltier element, that keeps the laser diode at a fixed temperature (20° C). Light is coupled into a single mode fibre (SMF) with collimating lenses (CL) before incident on the detection area of the powermeter.

A picture of the laser diode housing is shown below:

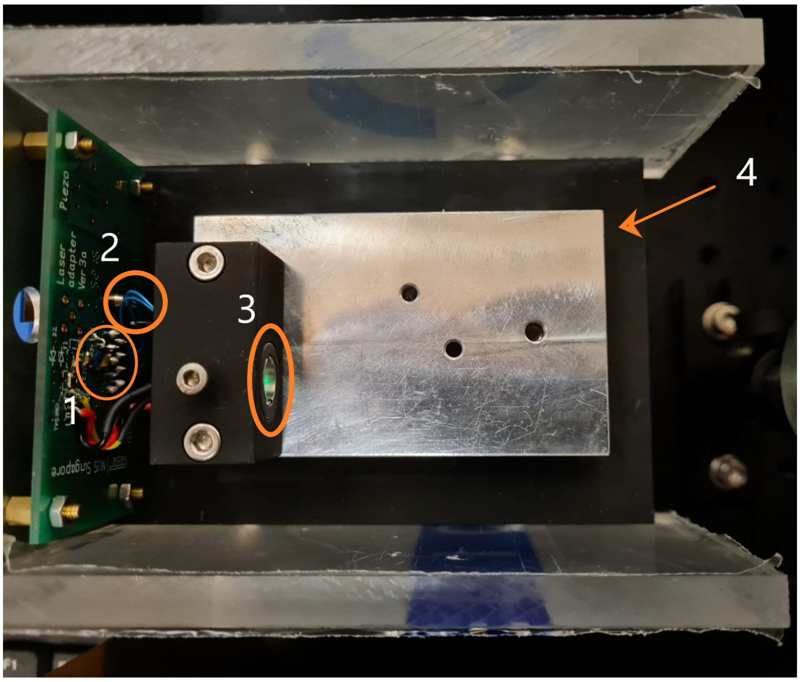

Fig. 1.8 Connection of the laser diode was via a 9-pin D-sub connector (1). Temperature control was done using a Proportional-Integral-Derivative loop controller connected to a Peltier element and a thermistor (blue wires, 2). The L515A1 laser diode (3) is housed inside a thermally conductive housing, which rests on top of another thermally conductive layer (aluminium base), which is on top of a peltier element, with the other side being a heat sink (black aluminium base, 4).

By varying the laser diode input current and measuring the output power upon conversion based on equation 1.14, we can obtain the results shown in **Fig.** 1.9.

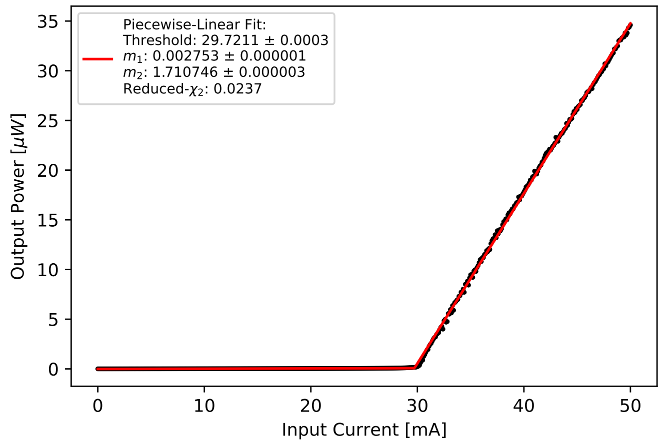

Fig. 1.9 Power output as measured using a Si photodiode, 0.1mA increments, range: 0-50mA

Power-current (P-I) measurements were done from the range of 0 - 50 mA in increments of 0.1 mA, with the process automated using a Python script. Comparing the P-I curve with the illustration in **Fig.** 1.6, we can see that the threshold is a bit higher than 30 mA. I attempted to use a piecewise-linear fit to the experimental data and obtained a threshold current value of about 29.7 mA. We can also take the logarithm of the output power:

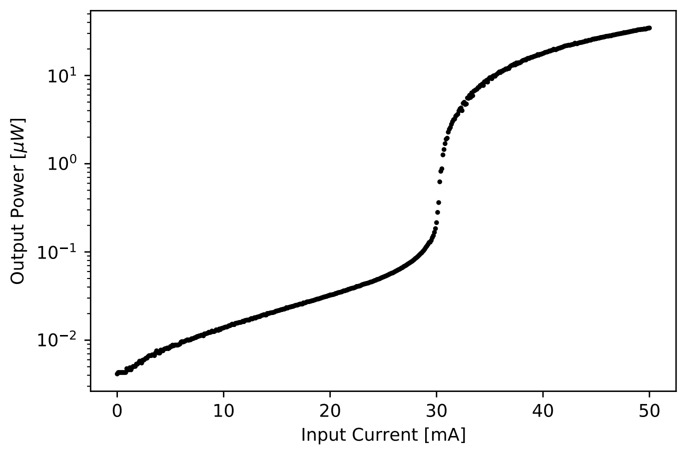

Fig. 1.10 Log-scaled output power. Range: 0-50 mA, 0.1 mA increments

From the log-scaled P-I curve, the steepest change (0.2 μW at 30 mA to 3.65 μW at 32 mA) in output power is around the range of 30 mA to 32 mA. The P-I curve offers a simple check on where the threshold could be.

1.2.2 Spectrum

The threshold of a semiconductor laser diode can also be determined by looking at the spectrum of the laser diode. As light from the laser diode transits from a broadband LED light to a narrowband "laser" light, we expect to see the linewidth (Full-Width at Half-Maximum, FWHM) of the spectrum decrease past the lasing threshold.

Using an OceanOptics USB-type reflective grating spectrometer, rated for operation in wavelengths between 399 nm and 731 nm, the spectrum of the laser diode for varying input currents was collected. At the lasing threshold, oscillation of a single resonant mode occurs, such that energy is only pumped into this mode above the threshold. This results in a narrow spectral linewidth (FWHM) past the threshold. Thus, by looking at the FWHM of the spectrum at each current value, we can determine the lasing threshold.

A convenient way at looking at the FWHM of a spectrum would be to fit a curve to the experimental data points and obtain the FWHM from the fitted plot. With a Gaussian amplitude fit:

$$f(x) = C_0 + A \cdot e^{-\frac{(x-\mu)^2}{2\sigma^2}} \tag{1.15}$$

where A, μ, σ are the amplitude, mean and standard deviation of the Gaussian curve respectively and C_0 is a constant. We can obtain the FWHM of the fitted curve via

$$FWHM = 2\sqrt{2ln2} \cdot \sigma \tag{1.16}$$

By varying the input current to the laser diode from 0 mA to 45 mA in 1 mA increments, fitting each spectrum to a Gaussian, we obtain:

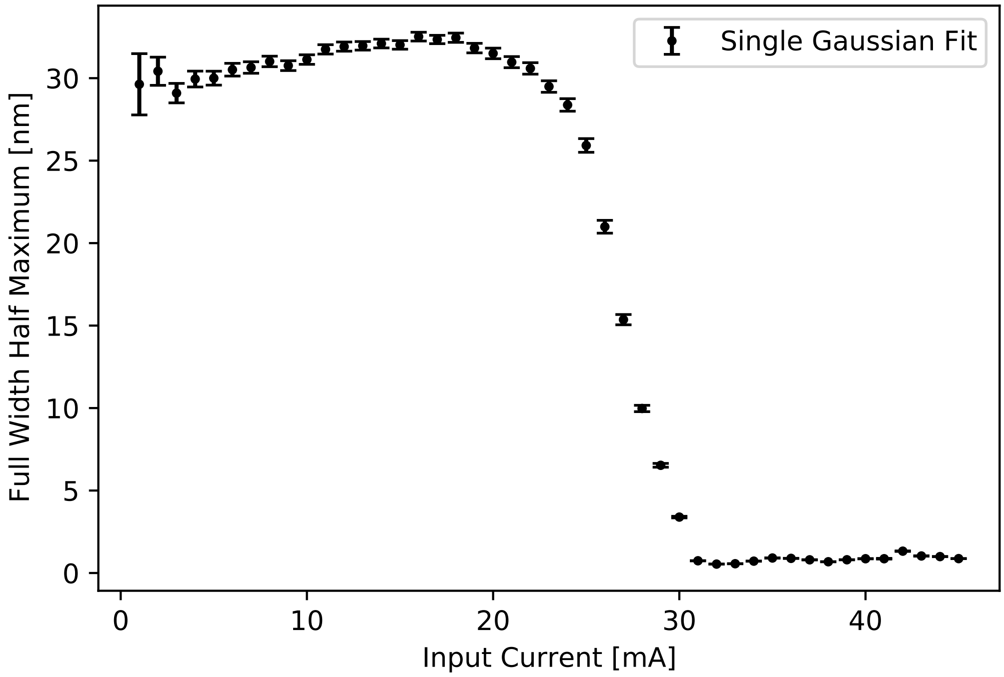

Fig. 1.11 Gaussian fit for data collected with OceanOptics USB spectrometer. 1 mA increments; 0-45 mA. Vertical error bars follows from error propagation from fitted values.

From figure 1.11, there are 2 clear regions that separate the input current values, one being the region lesser than 31 mA, and another region larger than 31 mA. The first region, or the region of spontaneous emission of the laser diode, the FWHM is tens of nm wide. The simulated emission region is where the FWHM is just about 1 nm wide, which is limited by the resolution of the spectrometer (about 1.5 nm). The transition between these 2 regions occurs in the range of 30-32 mA, which is similar to our power-current curve data.

In order to have a better confidence, we measure the spectrum in smaller increments of 0.1 mA instead, and the result is as follows:

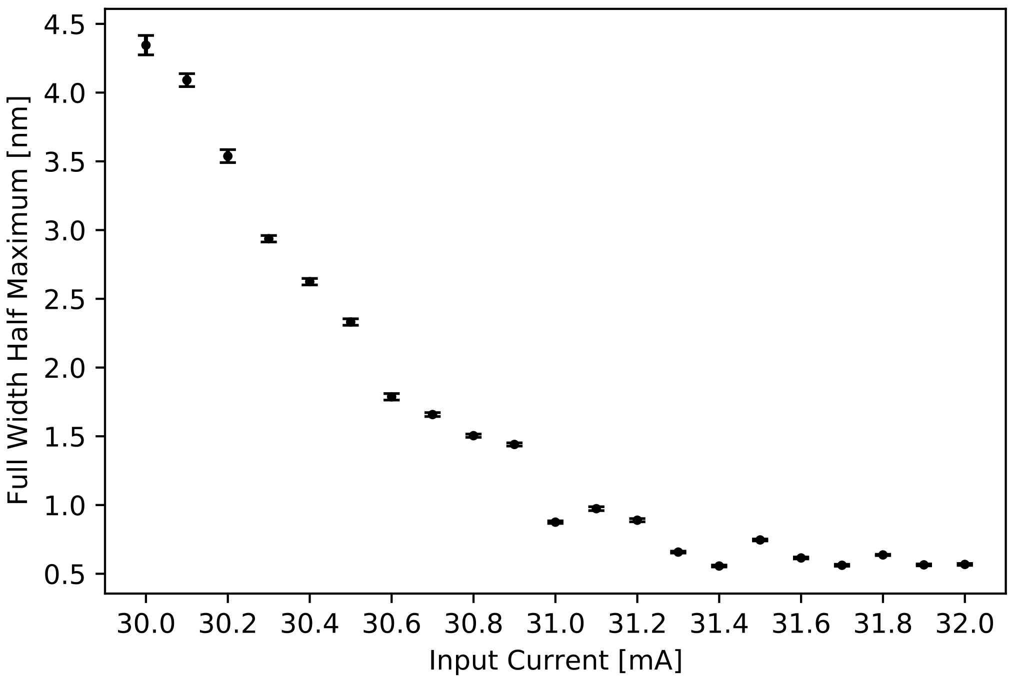

Fig. 1.12 Gaussian fit for data collected with OceanOptics USB spectrometer. Range: 30-32 mA, 0.1 mA increments

This suggests that the transition between spontaneous and stimulated emission of the laser diode, or threshold, occurs when the laser diode input current is around the 30.9 mA to 31.3 mA, as given by a more distinct drop in the FWHM from about 1.5 nm at 30.9 mA to less than 1 nm at 31 mA.

However, a Gaussian fit (single Gaussian to be specific) might not be the most appropriate fit, which can be seen visually when looking at the spectrum. We attempt to fit a double Gaussian instead, with the equation of fit given as:

$$h(x) = C_0 + A_1 \cdot e^{-\frac{(x-\mu_1)^2}{2\sigma_1^2}} + A_2 \cdot e^{-\frac{(x-\mu_2)^2}{2\sigma_2^2}}, \tag{1.17}$$

where the parameters are the same as for a single Gaussian fit, but now with two amplitudes, mean and standard deviations.

An example of the spectrum measured using the same spectrometer (OceanOptics), with a comparison between a single Gaussian fit and double Gaussian fit is shown below:

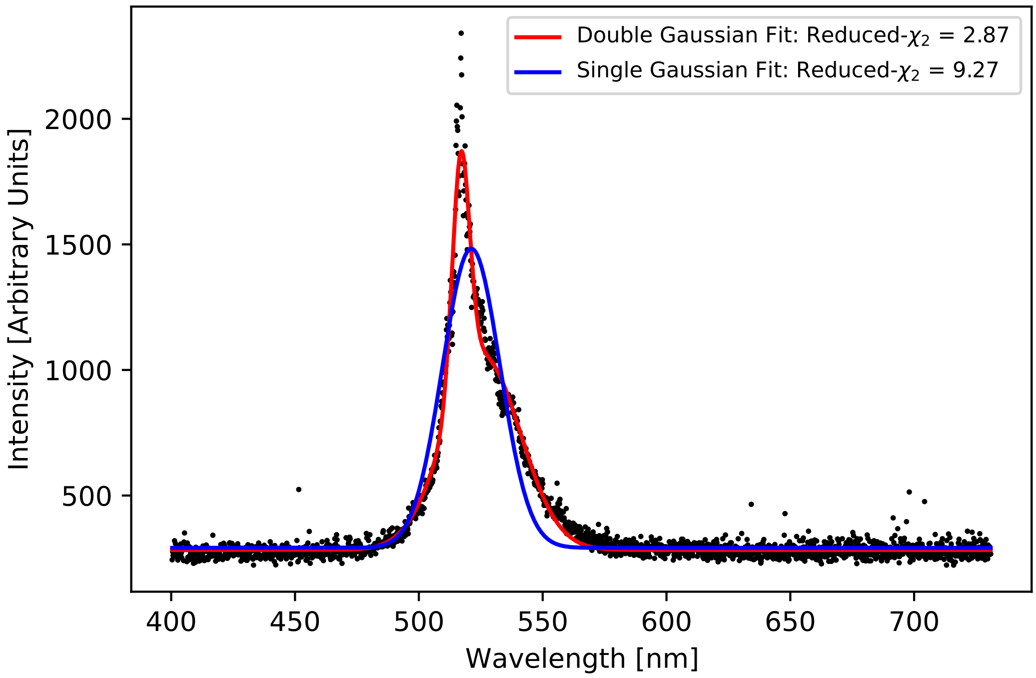

Fig. 1.13 Spectrum of light from L515A1 laser diode with an input current of 25 mA. The double Gaussian (red) has a lower reduced-χ_2 of 2.87, lower than 9.27 for a single Gaussian fit (blue). Consistently higher reduced-χ_2 is seen for a current values ranging from 10mA to about 31mA, where the spectrum was limited by the resolution of the spectrometer (1.5nm).

From **Fig.** 1.13, we can see that a single Gaussian fit does not fit well with the spectrum data. The better fit with a double Gaussian fit could suggest that there are two main emission spectrum, one being a broadband emission and the other corresponding to the resonant cavity frequency of the laser diode. For the spectrum for 25 mA (**Fig.** 1.13), with reference to equation (1.17), we obtain $A_1 = 771 \pm 7$, $\mu_1 = 525.7 \pm 0.1$ nm and $\sigma_1 = 15.2 \pm 0.1$ nm as the broadband spectrum. Value of $A_2 = 930 \pm 10$, $mu_2 = 516.94 \pm 0.04$ nm and $\sigma_2 = 3.50 \pm 0.05$ nm was obtained for the narrowband spectrum corresponding to the resonant cavity frequency of the laser diode. As the input current increases, the two peaks of a double gaussian fit moves towards a similar central wavelength of about 516 nm. Reduced-χ_2 values for single and double Gaussian fit are relatively similar as well. Additional spectrum fits for varying input currents can be found in Appendix A.

Note that in **Fig.** 1.13, there are some smaller peaks in the 450 nm, 650 nm and 700 nm range. They are present throughout the spectrum data collected within the same day, which could be due to noisy pixels on the imaging strip of the USB spectrometer, or constant ambient light from unknown sources. However, since these peaks are far away from the wavelength we are using (around 515 nm), we will ignore this.

Another way of measuring the FWHM would be to measure the full-width at half maximum, which is the half way mark between the data point with the highest intensity value and the mean ambient intensity value when the laser is off. By obtaining the width between the two points of intersection of the half-maximum horizontal line and the spectrum data, the FWHM can be calculated. An illustration is shown in **Fig.** 1.14.

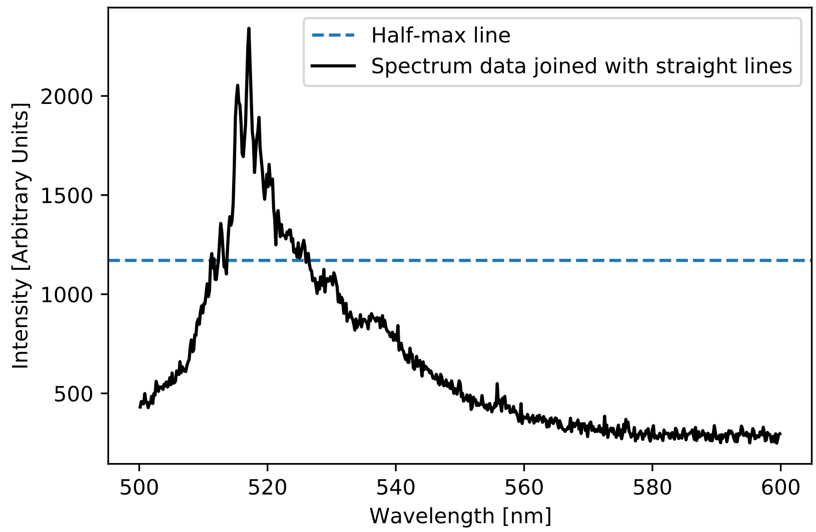

Fig. 1.14 Finding of FWHM via intersection of half-maximum line and spectrum data joined with straight lines. Example used is for 25mA as well. The FWHM obtained for this example is 7.75nm.

Applying this method and iterating with a script throughout the range of input current 0 - 50 mA in 1 mA as well as 30 - 36 mA in 0.1 mA increments, we obtain again a sharp drop in the FWHM values around the 31 mA mark (1 nm at 30.9 mA to 0.7 nm at 31 mA), as shown in **Fig.** 1.15.

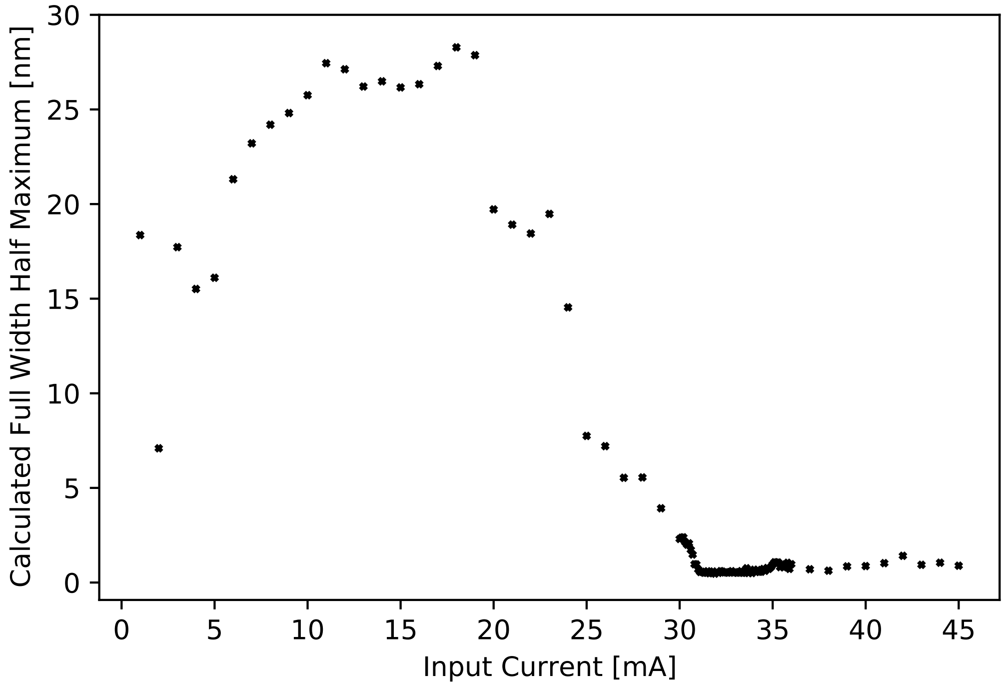

Fig. 1.15 FWHM obtained via intersection of half-maximum line and spectrum

Hence, we define 31 mA as the threshold current.

1.2.3 Power Spectral Density

The power spectral density of a thermal light source is related to its temperature in the relation:

$$S(\nu) = \frac{h\nu}{\exp(h\nu/k_B T) - 1} \tag{1.18}$$

In order to generate thermal light that has a high spectral distribution, we require light from the laser diode to have a high power output and a narrow linewidth, while still below the threshold current. Thus, we intend to run the laser diode at below 31 mA to maximise the spectral distribution while still being a thermal light source.

Chapter 2

Temporal Correlation of Light

With the semiconductor laser diode running at below threshold, we expect there to be bunching ($g^{(2)}(\tau = 0) > 1$). We proceed with measurements of temporal second order correlation.

2.1 Temporal $g^{(2)}$ Measurements

For measurements of $g^{(2)}(\tau)$, we improve on the setup from **Fig.** 1.2.

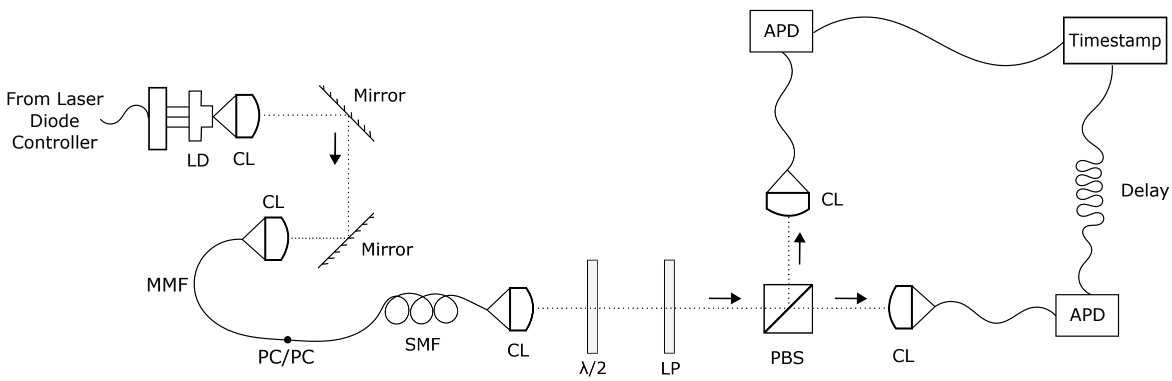

Fig. 2.1 Setup for $g^{(2)}(\tau)$ measurements. Flow of the setup is explained further below.

With reference to **Fig.** 2.1, the flow of the setup is as such. A semiconductor laser diode (LD) from ThorLabs (model L515A1), with a manufacturer-stated centre wavelength of 515 nm at 25°C, is connected to a laser diode controller unit. The laser diode controller is a field-programmable gate array (FPGA) unit capable of controlling the input current supplied to the laser diode, as well as temperature control through the use of a thermoelectric peltier element and a thermistor. The voltage across the peltier element is adjusted with a PID loop, based on temperatures measured by the thermistor. Temperature of the laser diode was kept at 20°C.

Light from the laser diode is collimated using an aspheric collimating lens (CL) before reaching two mirrors. The combination of two mirrors, each on a tip-tilt mount, allows for four degrees of freedom when coupling laser diode light into the multi-mode fibre (MMF), which is connected to a single mode fibre (SMF) with a flat physical contact mating sleeve (PC/PC).

The choice of using a single mode fibre is to select a single spatial mode of light from the laser diode. The temporal second order correlation function can also be given by [15] as:

$$g^{(2)}(\tau) = 1 + \beta |g^{(1)}(\tau)|^2, \tag{2.1}$$

where $\beta = 1/M$ is a factor accounting for the loss of coherence due to a number M of spatial and polarization modes. For single polarization light from a point source (such as an unresolved star), M takes the value of 1. Thus, the theoretical value at zero delay is $g^{(2)}(\tau = 0) = 2$, or the contrast $C = g^{(2)}(0) - 1$ is 1 for a spatially coherent source. In order to maximise the $g^{(2)}$ signature, we select a single spatial mode using the single mode fibre. Due to experimental equipment being imperfect, as per all other equipment, we do not expect the single mode fibre to only allow a single spatial mode to pass through.

Continuing the flow of the setup, a half-wave plate ($^{\lambda}/_{2}$-plate), when paired with a linear polariser (LP), balances and maximises the count rates at each avalanche photodiode (APD) respectively. Since the light from the laser diode is linearly polarised, the linear polariser was first inserted to maximise counts on both the reflected paths of the polarising beam splitter (PBS), before the half-wave plate is rotated to balance the counts. Reason behind the need to balance count rates in both reflected and transmitted arms is to maximise the coincidence counts. As mentioned in the earlier section, the need to split the beam into two separate paths is to account for the dead time of the other detector. The APDs are electronically connected via BNC cables to a timestamp unit which timestamps photoevents. One of the APD has an additional 13 m of coaxial cable, which introduces a timing delay of about 65 ns. This is to account for the dead time of the timestamp unit of about 2 ns.

The APD used is a passively quenched Perkin Elmer C30902S, which has a timing resolution (FWHM) of about 1.2 ns [12].

Results and Discussion

With the setup as shown in **Fig.** 2.1, temporal second order correlation data was obtained after running a script that translated timestamp information to coincidence events, as well as the normalised coincidence events. Once again, for a Lorentzian linewidth bunched light, the equation is given by equation (1.9). Running measurements for the laser diode with input current ranging from 28 mA to 33 mA in 1 mA increments, an example plot for a current value of 30 mA with a linear fit is shown below:

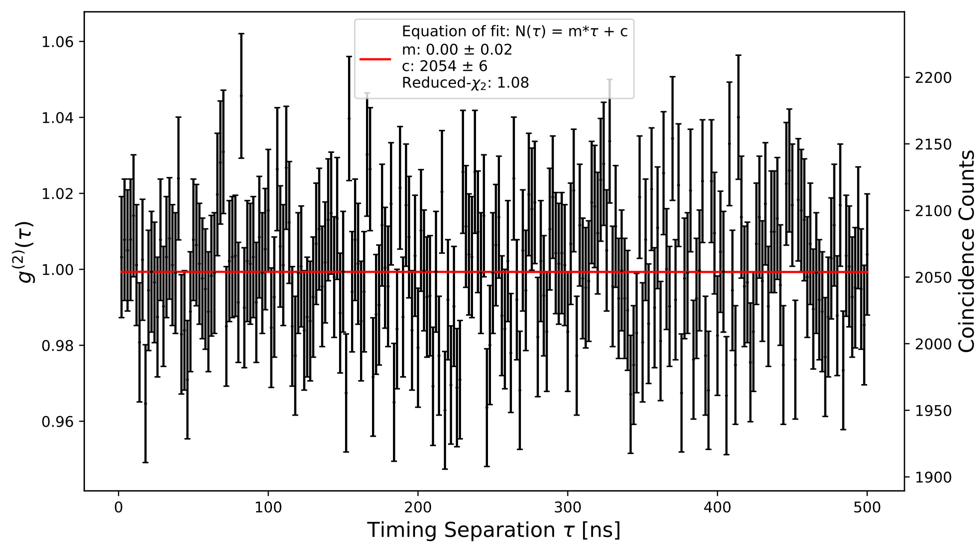

Fig. 2.2 Temporal second order correlation with an input current of 30 mA (below threshold current of 31 mA). Vertical error bars are assumed to be Poissonian (ie. square root of the coincidence count at a data point). Equation of fit used is a linear fit. Comparison with a exponential fit in equation (1.9) led to fitting errors, which prompted me to fit with a linear fit.

With reference to **Fig.** 2.2, we can see that a linear fit returns us a $g^{(2)}(\tau)$ value of roughly 1 throughout the range of 0 ns to 500 ns, with a majority of data points within 1σ poissonian noise deviation from the equation of fit. There is however, a possible peak of $g^{(2)} = 1.05$ at when of $\tau = 80$ ns, but since it is about 15 ns (corresponds to a

3 m electronic delay, as electronic signals move at two-thirds the speed of light in BNC cables) away from the expected bunching location (65 ns), we do not consider it as possible bunching of light from the laser diode at 30 mA.

While a linear fit might be more suitable than an exponential fit in this case, we also note that there are possible periodic patterns in the plot of $g^{(2)}(\tau)$ in the order of about 100 ns.

The second order temporal correlation function $g^{(2)}(\tau)$ is also related to the timing resolution of the detectors used as given by [16] as:

$$g^{(2)}(\tau = 0) - 1 \propto \frac{\tau_c}{\tau_t}, \tag{2.2}$$

where τ_t refers to the timing resolution of the detector used (1.2 ns for C30902S APD) and τ_c, as mentioned in the earlier section, is the coherence time of the light. We suspect that it could be due to a low ratio of τ_c/τ_t.

Based on the relation seen in equation (2.2) and noting that for the setup as shown in **Fig.** 2.1 returns a $g^{(2)}(\tau) = 1$, we attempt to increase the coherence time of the light from the laser diode.

2.2 Spectral Filtering

2.2.1 Coherence Time of Light

The coherence time of a light source can be determined from the spectral bandwidth itself, which is again given by the Wiener-Khintchine Theorem [2, 3]. For a light with a Lorentzian lineshape:

$$S(\omega) = \frac{1}{\pi} \frac{\Delta\omega/2}{(\omega - \omega_0)^2 + (\Delta\omega/2)^2}, \tag{2.3}$$

the Fourier transform returns us an exponential distribution with the form:

$$\mathcal{F}\{S(\omega)\} = e^{-i2\pi\tau\omega_0 - \Delta\omega\pi|\tau|} = g^{(1)}(\tau), \tag{2.4}$$

where the FWHM, $\Delta\omega$ is the linewidth of a Lorentzian profile, and the equality to $g^{(1)}(\tau)$ given by Wiener-Khintchine Theorem. By comparing with the Siegert relation in equation (1.10), we obtain

$$g^{(2)}(\tau) = 1 + e^{\frac{-2|\tau|}{\tau_c}}, \tag{2.5}$$

where the coherence time τ_c for a Lorentzian spectral profile is

$$\tau_c = \frac{1}{\pi \Delta\omega}. \tag{2.6}$$

For a Gaussian lineshape, the coherence time τ_c is given as [10]:

$$\tau_c = \frac{\sqrt{8\pi ln2}}{\Delta\omega} \tag{2.7}$$

From the Gaussian and Lorentzian lineshapes, the coherence time is inversely proportional to the spectral bandwidth of the light

$$\tau_c \propto \frac{1}{\Delta\omega} \tag{2.8}$$

Thus, to increase the coherence time of the light from the laser diode, we do spectral filtering to reduce the linewidth.

2.2.2 Optical Bandpass Filter

Optical bandpass filters work by transmitting only selected wavelengths of light, while absorbing other wavelengths using multiple layers of substrates of varying thickness. Passing broadband light through an optical bandpass filter effectively reduces the linewidth of the light, depending on the FWHM of the filter.

Using a optical bandpass filter (model NT43-125 from EdmundOptics) with a manufacturer stated centre wavelength of 546 nm and a FWHM of 10 nm, we measure the spectrum after passing laser diode light through it.

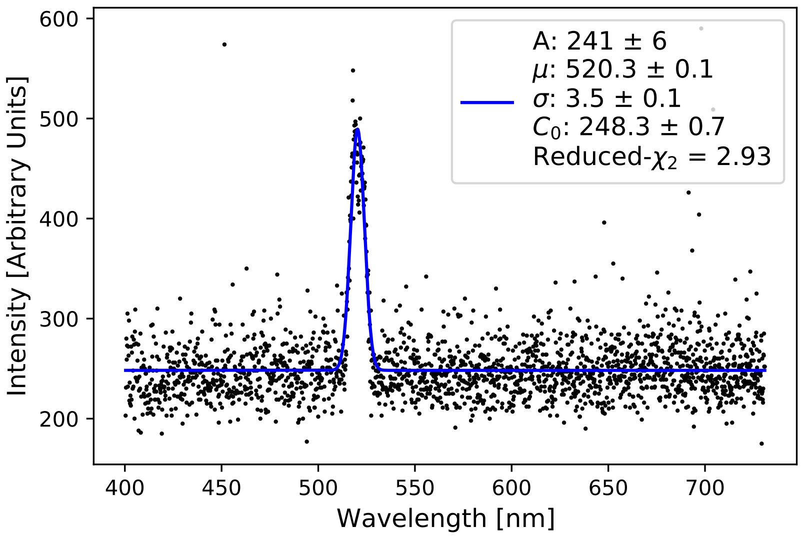

Fig. 2.3 Spectrum measured by reflective grating spectrometer (1.5nm resolution) after a bandpass filter. Laser diode at an input current of 25 mA. Bandpass tilted at an angle of about 25° from the incident light.

We fit the spectrum with a single Gaussian fit like in equation (1.15), and obtained a fitted FWHM of 8.2 ± 0.2 nm. At 25 mA, the FWHM without an optical bandpass filter has a fitted value of 25.9 ± 0.4 nm as seen in section 1.2.2.

A spectral FWHM of 8.2 nm corresponds to a subsequent coherence time τ_c of 0.45 ps, which is still three to four orders of magnitude lower than the timing resolution of the APDs (1.2 ns). Thus, we require other methods to reduce the linewidth.

Note that while the optical bandpass filter is insufficient in reducing linewidth, it will be used to suppress optical crosstalk due to breakdown flash of the APDs, which has wavelengths in the range of 850 nm [17].

2.2.3 Solid Etalons

A solid etalon is a piece of high refractive index material that acts as a frequency comb, allowing only certain frequencies of light to transmit through the etalon, which has highly reflective coatings on the inner walls. The thickness of the etalon L determines the number of interference modes m of vacuum wavelength λ_0 that can be present inside the etalon medium with refractive index n in the relation [18]:

$$m = \frac{2nL}{\lambda_0}. \tag{2.9}$$

The transmission peaks of the etalon are separated in frequency by the free spectral range (FSR):

$$FSR = \frac{c}{2nL} \tag{2.10}$$

where c is the speed of light in vacuum. A simple illustration below identifies the free spectral range.

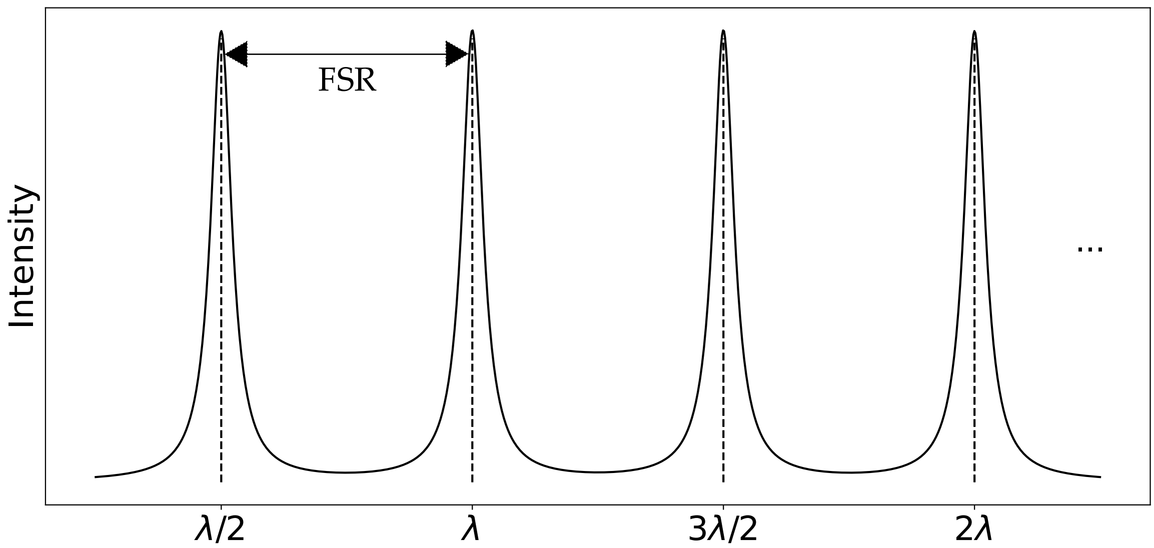

Fig. 2.4 Transmission through a solid etalon. Peak to peak separations are the free spectral range (FSR), while λ refers to the wavelength of the transmitted light, which are integer multiples of half-wavelengths.

With the solid etalon, there would only be light transmitting through when the emission spectrum of the laser diode coincides with the transmission peak of the etalon. The etalon effectively acts as a spectral filter to select longitudinal modes of the laser diode when we vary the transmission frequency, which we shall term as frequency tuning.

Frequency tuning of etalons can be done by tilting the etalons as well as temperature tuning [18]. In order to avoid losses [19] and frequency-walkoff [20] from tilting of the etalon, we decided on frequency tuning with temperature.

Sellmeier Coefficients

In order vary the transmission peaks of the etalon, we refer back to equation (2.10). Both refractive index n and thickness of the etalon L are both temperature dependent.

In addition to temperature dependence, n varies with wavelength λ as well, which is given by the wavelength-dependent Sellmeier equation [21]:

$$n^2(\lambda) = 1 + \sum_i \frac{B_i \lambda^2}{\lambda^2 - C_i} \tag{2.11}$$

where B_i and C_i are the experimentally derived Sellmeier coefficients, and λ is the wavelength of light in the medium. By taking the derivative of equation (2.11) with respect to temperature, we can arrive at the wavelength-temperature-dependent Sellmeier equation:

$$\frac{dn(\lambda,T)}{dT} = \frac{n^2(\lambda,T) - 1}{2 \cdot n(\lambda,T)} \left(D_0 \cdot \Delta T + D_1 \cdot \Delta T^2 + D_2 \cdot \Delta T^3 + \frac{E_0 \cdot \Delta T + E_1 \cdot \Delta T^2}{\lambda^2 - \lambda_{TK}^2} \right), \tag{2.12}$$

where D_0, D_1, D_2, E_0, E_1 and λ_{TK} are again experimentally derived coefficients. Along with the thermal expansion coefficient of the substrate, we can obtain the dependence of free spectral range (FSR) on temperature, which can then be used to calculate the tuning rate, depending on the material used. For specific calculations for the type of etalon medium used, refer to Appendix B.

Results and Discussion

With a choice of a 1 mm thick etalon made of Suprasil 311, a type of fused silica glass with low impurities, the tuning rate is calculated to be about -4 GHz/K. We insert the etalon into the setup as such:

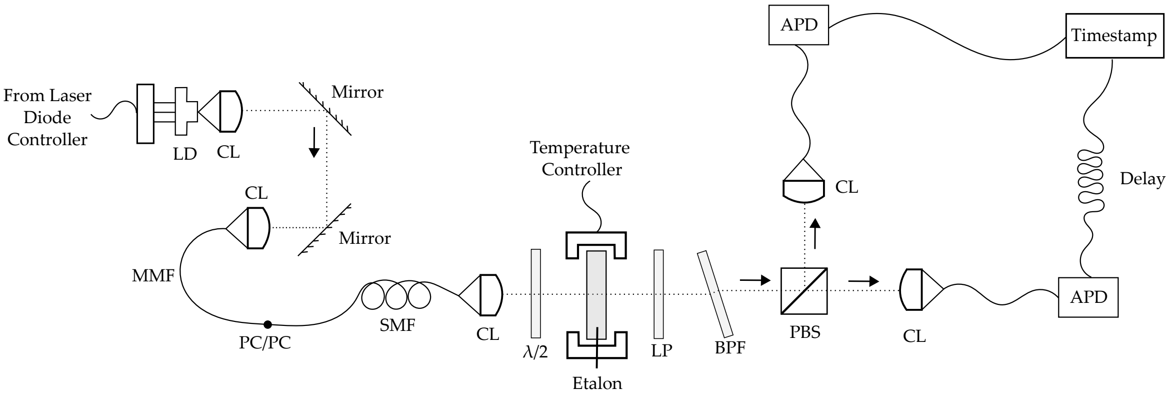

Fig. 2.5 Spectral filtering with 1 mm thick solid etalon for $g^{(2)}(\tau)$ measurements. Etalon is placed such that the back-reflection off its surface coincides with the downstream laser diode light, which maximises interference inside the etalon and therefore higher transmission ratios. Refer to Appendix A for a photo of the setup.

With the experimental setup in **Fig.** 2.5, the etalons were heated at a constant voltage through the use of 2 through-hole resistors rated 30 W arranged in parallel. A thermistor was also placed close to the etalon itself and held in place with epoxy glue. A picture of the etalon holder with a 1mm etalon in place is shown below.

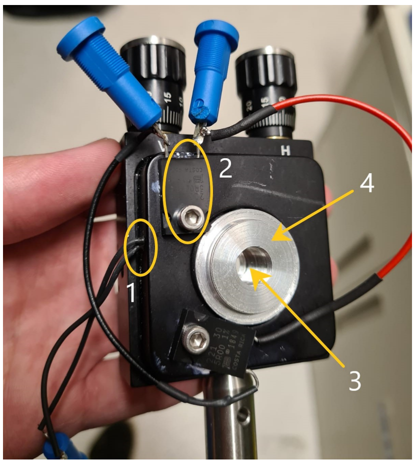

Fig. 2.6 Etalon holder with thermistor (1) and two 30 W through-hole resistors (2). The 1 mm etalon (3) is held in place with an aluminium ring (4), which reduces direct air contact with the etalon, which can result in temperature fluctuations.

In order to determine the thermal response of the etalon holder, we measure the temperature change as registered by the thermistor with time. The resulting plot is as such:

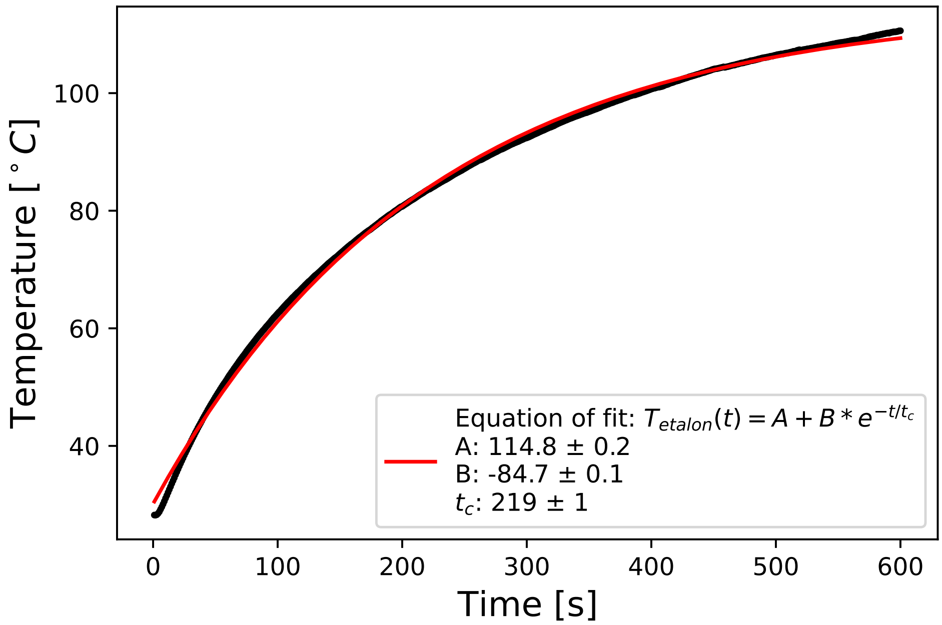

Fig. 2.7 Heating curve of etalon at constant 10 V. Time constant t_c was about 219 s. Black points are experimental data while the red curve is the fitted curve.

With a heating time constant of (219 ± 1) s, the etalon holder requires just about 10 s for a temperature increase of 13% between the starting and final temperatures. From the same figure, we can also see that there is a slight delay of about 5 s between the start of the heating process (t =0) and the time where we see an increase in the temperature. This could give a rough idea of the thermal lag of the etalon holder itself. However, this could also be contributed by the delay in data collection process (writing and reading of data).

Recalling that the tuning rate is about -4 GHz/K, we heat the etalon holder containing a 1 mm thick etalon at a constant 10 V. By varying the temperature of the etalon, we scan through the spectrum of the light source at the particular input current. An example of heating of etalons to scan through the spectrum can be shown in **Fig.** 2.8. For the 1 mm etalon, the free spectral range (FSR) according to equation (2.10) to be about 100 GHz.

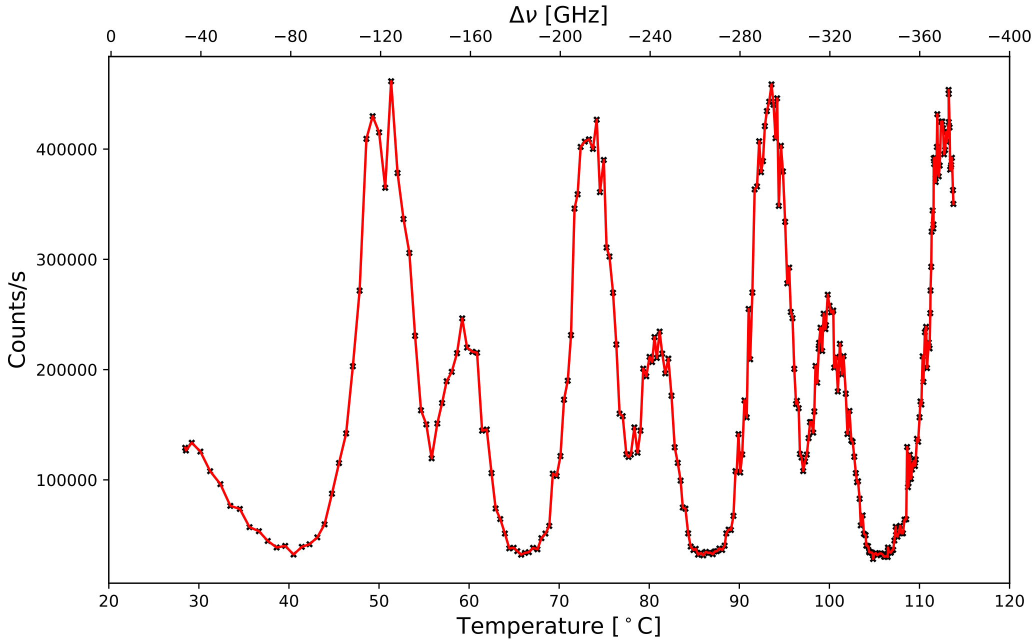

Fig. 2.8 Scanning of spectrum at 35 mA (above threshold) with etalon heating at a constant 10 V. Crosses (black) indicate experimental data collected that are joined by straight lines (red). Temperature range of 30° C to 115° C, which covers more than 3 FSR (100GHz) of the 1mm etalon. Note that the linewidth of the light at 35 mA is tens of GHz wide, or *pm* wide, which is better than the resolution limit of a reflective grating spectrometer.

By setting the input current at 35 mA, which is above the threshold of about 31 mA, we demonstrate the ability of etalon tuning as a way to observe the spectrum to a precision better than the USB type spectrometer used previously.

By scanning the spectrum for current values slightly below the threshold current of about 31mA, we record the $g^{(2)}(\tau)$ after setting the temperature that corresponds to one of the spectrum peaks (ie. obtain back the peak counts) just like in **Fig.** 2.8. Setting of temperatures was done with the use of a proportional–integral–derivative (PID) controller, which adjusts the output voltage to the heating resistors based on the temperature values detected at the thermistor.

The temporal second order correlation function $g^{(2)}(\tau)$ plot is fitted to the equation:

$$N(\tau) = A + B \cdot e^{-\frac{2|\tau|}{\tau_c}}, \tag{2.13}$$

where τ is the timing separation between photoevents and τ_c the coherence time. The normalised factor $\frac{B}{A}$ is the correlation factor. Should there be no correlation, $\frac{B}{A}$ would be close to 0, while a perfect correlation returns a ratio of 1. $g^{(2)}(\tau = 0)$ is obtained by normalising equation (2.13) by A, or the ratio of $1 + \frac{B}{A}$.

The process of adjusting the set temperature and looking at the $g^{(2)}(\tau)$ plot is done concurrently. Once a set temperature with the highest $g^{(2)}(\tau = 0)$ is obtained, we adjust the laser diode input current. The resulting $g^{(2)}(\tau = 0)$ against current values in the range of 30.3 mA to 30.6 mA is as such:

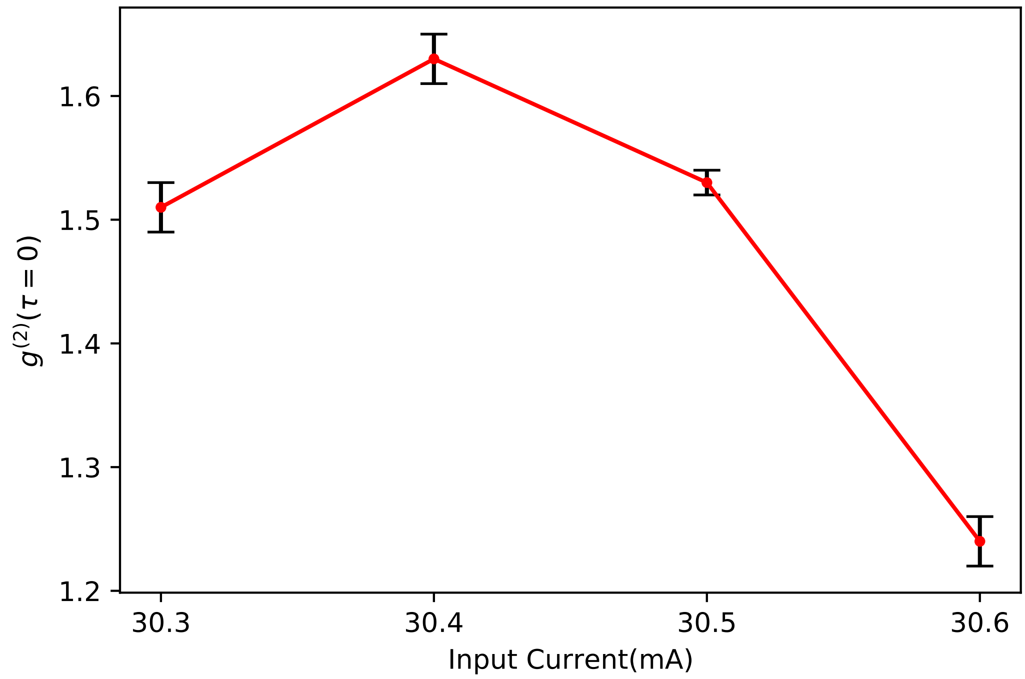

Fig. 2.9 $g^{(2)}(\tau = 0)$ values with varying current after temperature tuning of the etalons. Error bars are shown in black. For varying input currents of 30.3 mA to 30.6 mA in increments of 0.1 mA with etalon at $T_{etalon} = 42.450°C$, the highest $g^{(2)}(\tau = 0)$ value is when input current is 30.4 mA.

The $g^{(2)}(\tau)$ plot for the laser diode input current of 30.4 mA (corresponding to the maximum $g^{(2)}(\tau = 0)$) is shown as such:

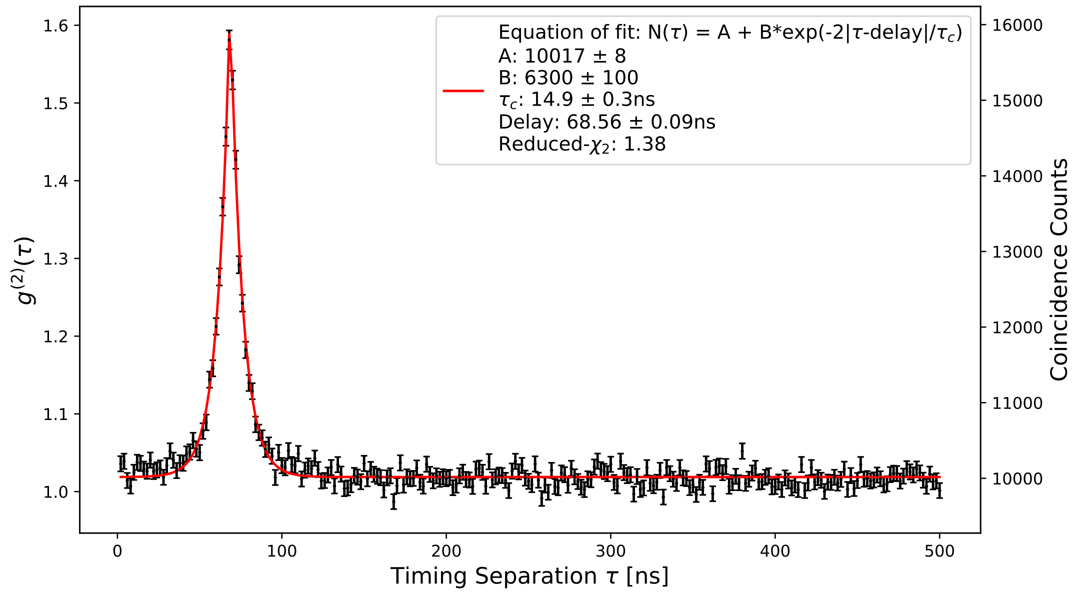

Fig. 2.10 Temporal correlation with laser diode input of $30.4mA$, with a set temperature of $42.450°C$. Fitted values using equation 1.9 returns a coherence time of 14.9 ns with peak $g^{(2)}(\tau)$ of 1.63. Error bars are again assumed to be Poissonian.

From **Fig.** 2.10, the fitted curve based on equation (2.13) returns us a normalised $g^{(2)}(\tau = 0)$ of 1.63 ± 0.02, with a coherence time of 14.9 ± 0.3 ns.The delay given by the fit was at 68.56 ± 0.09 ns, which is close to where we expect the bunching signal to appear, given the 13 m coaxial cable used for the electronic delay. Electronic signals in coaxial cables travel at two-thirds the speed of light in vacuum, thus a 13 m coaxial corresponds to roughly 65 ns of delay. The additional 3 ns could be due to the extra time delay contributions from the BNC connectors, or from slightly different optical path lengths (in the order of cm).

The $g^{(2)}(\tau = 0)$ of the laser diode running at 30.4 mA does not peak at a value of 2 like in **Fig.** 1.4 for bunched light, which could be due to the presence of more than one spatial mode and/or polarisation mode, as seen in equation (2.1). Noting down the set temperature of the 1 mm etalon T_{etalon} of 42.450°C as well as the input current of 30.4 mA, we proceed with spatial second order correlation measurements.

Chapter 3

Spatial Correlation of Light

By observing the correlation of intensities from the same light source at different points in the space transverse to propagation of light, we can retrieve spatial information of the light source. For a spatially incoherent, uniform intensity, circular, quasi-monochromatic light source, this relation is once again justified by the van-Cittert Zernike theorem with the Siegert relation as:

$$g^{(2)}(b,\tau=0) = 1 + \left|\frac{2J_1(\pi\theta_{UD}b/\lambda_0)}{\pi\theta_{UD}b/\lambda_0}\right|^2, \tag{3.1}$$

where J_1 is the first order Bessel function of the first kind, θ_{UD} the angular diameter of the source, $b = |r_1 - r_2|$ the baseline and λ_0 the wavelength of light involved. In the previous chapter, we achieved a bunching peak value of $g^{(2)}(b=0,\tau=0)$ of 1.63. With reference to **Fig.** 1.5, as we increase the distance between each detector arm, we expect to see the correlation of intensities decay to a minimum. As such, we have to modify the setup to allow for the detectors to be translated in the direction transverse to propogation of light.

For the equation above to hold, we need a circular light source that is uniformly illuminated. Thus, we choose to use a pinhole aperture with collimated light from the laser diode incident on it. For a check of collimation, we refer to the Rayleigh length z_R

$$z_R = \frac{\pi\omega_0^2}{\lambda}, \tag{3.2}$$

within which a Gaussian beam has a relatively constant beam size. ω_0 refers to the beam waist (or the size of the light beam at its narrowest point) and λ referring to the wavelength of light involved. For our setup, which will be discussed further later in this section, we obtain a Rayleigh range of about 143 m with a beam size of about 5 mm.

The transverse coherence length, l_c, of a circular light source is given by as

$$l_c = \frac{\lambda z}{2R}, \tag{3.3}$$

where λ refers to the wavelength of light involved, z the distance from the light source and R the radius of the circular light source. As the distance between detectors increase beyond the transverse coherence length, the spatial coherence decreases to 0. In order to extract spatial information from the light source, the aperture size of the detector has to be smaller than the transverse coherence length, which sets a limit on the aperture size of the detector.

Lastly, to prove the concept of intensity interferometry using spatial second order correlation, we would require the aperture size of the detectors to be sufficiently small, such that it will not be able to resolve the source itself. With these additional constraints to our setup, we proceed to the experimental setup.

3.1 Setup for Spatial Correlation Measurements

Based on the options available in the lab, we settled on a 150 μm pinhole (Thorlabs P150S), with a quoted 150 $\pm$ 6 μm diameter. With this choice of aperture, we setup the experiment as such:

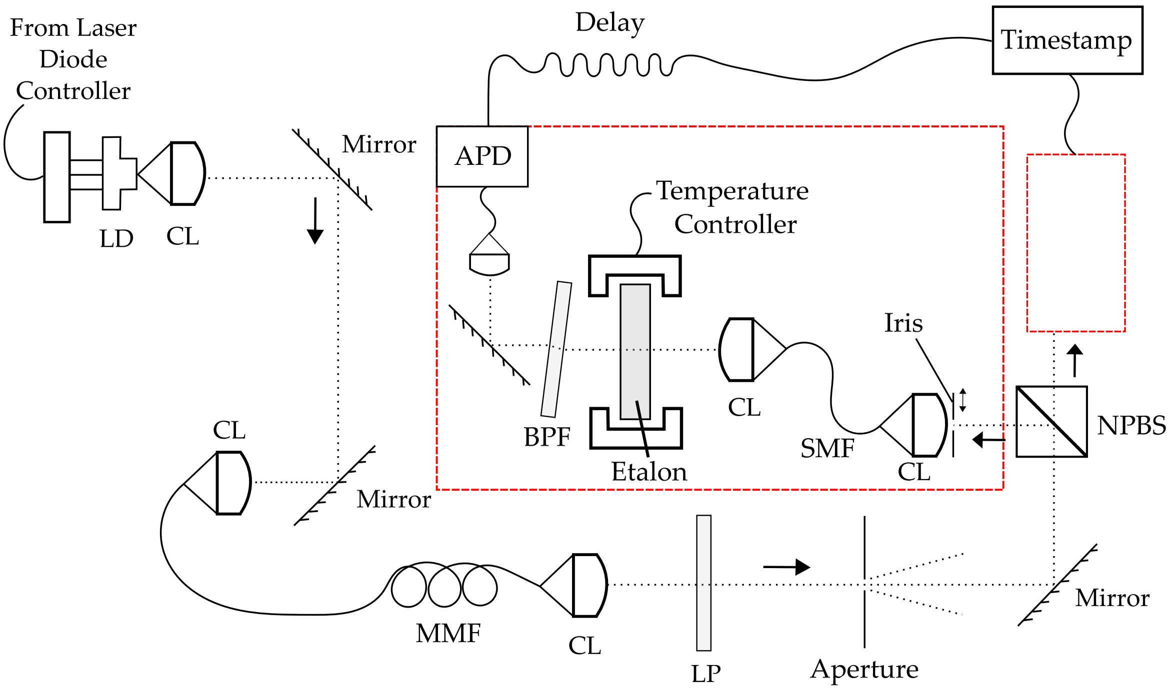

Fig. 3.1 Experimental setup for spatial second order correlation measurements. Aperture used is a 150 μm pinhole; iris used is 1 mm wide; distance from source to detection z: 0.50 m. Refer to Appendix A for a photo of the setup.

With reference to **Fig.** 3.1, we chose to use only the multimode fibre (MMF) before the aperture as we want to avoid the spatial coherence present from the output of a single mode fibre (SMF). Instead, light after passing through the MMF is collimated with an aspheric lens (Thorlabs C220B) with an effective focal length of 11 mm, and incident on a linear polariser (LP), before it is incident on the 150 μm pinhole. The pinhole then acts as a spatial mode selector, similar to how the slit after the light source in a Young's double slit experiment creates a spatially incoherent light source. Light after the pinhole is divergent, with an angle of divergence of about 1°. It is then incident on a non-polarising beam splitter (NPBS), which splits light into two directions, with each having a similar setup as the other (indicated by the red boxes). At a distance of about 50 cm away from the 150 μm pinhole, light is then incident on a 1 mm wide iris.

For a 150 μm light source at a distance of 50 cm away, the transverse coherence length is given by

$$\begin{aligned} l_c &= \frac{\lambda z}{2R} \\ &= \frac{(515\,nm)(50\,cm)}{150\,\mu m} \\ &\approx 1.7\,mm \end{aligned}$$

A 1 mm iris which limits the detector aperture size to 1 mm is lesser than the transverse coherence length. In addition, the 150 μm light source at a distance of 50 cm away spans an angular separation of approximately $3 \cdot 10^{-4}$ radians, which cannot be resolved by a 1 mm aperture according to Rayleigh's Criterion for visible wavelengths.

The 1 mm iris on each arm (reflected/transmitted), mounted on a X-Y translation stage, selects a spatial part of the light and is coupled into a single mode fibre (SMF) with an aspheric lens (Thorlabs C230B). Light from the other end of the fibre is normally incident on a 1 mm etalon, just like we did for the temporal second order correlation measurements, before passing through a bandpass filter (centre wavelength: 546 nm $\pm$ 5 nm) before being collected into a MMF connected to an avalanche photodiode (APD, passively quenched).

We first do a preliminary check if there is any bunching corresponding to $b = 0$ separation, or in other words, the temporal second order correlation. On the reflected arm of the setup in **Fig.** 3.1, we replace the single detector with another NPBS and two APDs for a temporal second order correlation measurement. We also remove the 150 μm pinhole and 1 mm iris for a similar setup for our temporal second order correlation measurements.

3.2 Results and Discussion

The results of the temporal second order correlation without pinhole and iris was as such:

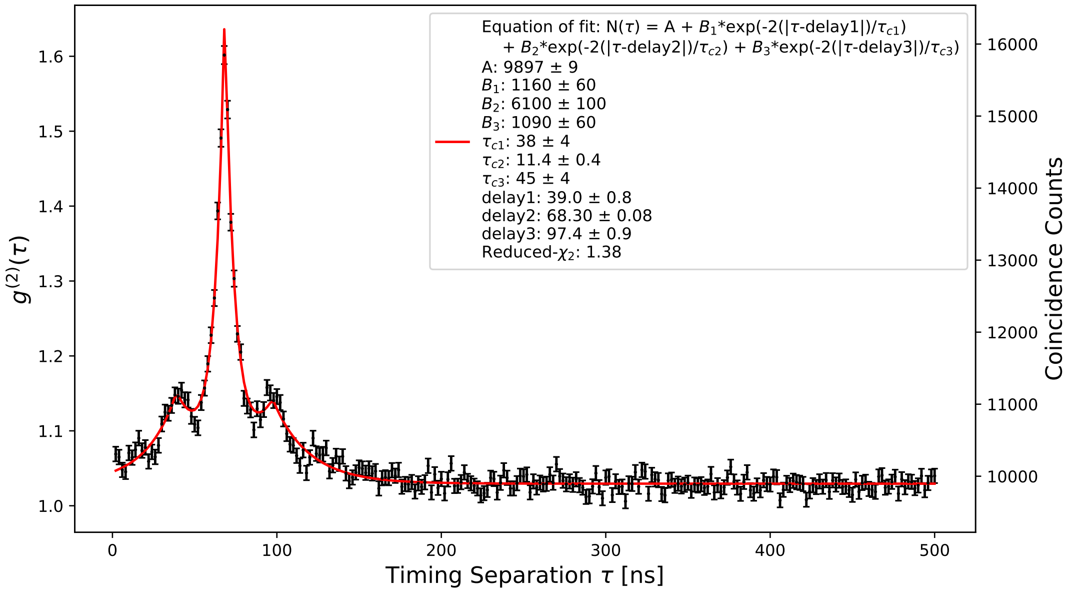

Fig. 3.2 Temporal second order correlation measurement as a preliminary check with no pinhole and iris. $T_{etalon} = 42.200°$C, laser input current: 30.4 mA

While we were still able to obtain a $g^{(2)}(b = 0, \tau = 0)$ of about 1.6, there were two additional distinct peaks with a smaller amplitude, symmetric about the main peak. Repeated measurements gave a similar result. Instead of fitting the plot with the same equation of fit as in (1.9), we introduce two additional terms in an attempt to get more information for the two extra peaks:

$$N(\tau) = A + B_1 \cdot e^{\frac{-2|\tau - delay1|}{\tau_{c1}}} + B_2 \cdot e^{\frac{-2|\tau - delay2|}{\tau_{c2}}} + B_3 \cdot e^{\frac{-2|\tau - delay3|}{\tau_{c3}}}, \tag{3.4}$$

where the two additional terms are also modelled the same as the central peak. Based on the equation of fit in (3.4), we obtain a $g^{(2)}(\tau = 0)$ of 1.61 ± 0.01 for the central bunching peak, with a coherence time of 11.4 ± 0.4 ns. For the side bunching peaks, the corresponding $g^{(2)}(\tau = 0)$ are 1.12 ± 0.01 and 1.11 ± 0.01 for the left and right peaks respectively, with coherence time of about 40 ns for both. They are also present at about 29 ns before and after the main bunching signature at the $\tau = 68$ ns mark. A 29 ns delay corresponds to a free space optical path difference of 8.7 m, which is longer than the path of the setup. The differences in this setup from the setup for temporal second order correlation measurements include the absence of a half-wave plate, position of linear polariser and the use of non-polarising beam splitters. We suspect that the additional bunching peak is a result of back reflection off an optical element such as the beam splitter, resulting in interference with the light propagating down the setup, causing delayed coincidence events.

We also note that for this measurement, a set temperature of 42.200 °C was used to tune the etalon to the peak count rates, corresponding to the emission peak of the light source, instead of a previous value of 42.450 °C. This could indicate that the emission peaks of the laser diode shift over time (measurements was done about 1-2 weeks apart), which would mean that temperature tuning of etalons before the start of measurements has to be done.

The 150 μm pinhole was then inserted in the path as indicated in **Fig.** 3.1. However, due to divergence of light after passing through the pinhole, the coupling into the collimating lens after the NPBS is inefficient. For the experimental setup in **Fig.** 3.1, we were only able to achieve a transmission ratio of about 0.1% when comparing the light intensity before the 1 mm iris and after the single mode fibre (SMF) with a powermeter. After passing through the etalon and optical bandpass filter, the count rates at each detector was essentially the dark counts of the detector ($\approx$1300 counts/s and $\approx$4200 counts/s for the two passively-quenched Silicon-APDs).

3.2.1 Challenges

Thermal Crosstalk between Etalons

One challenge with having one or more etalons in each arm of the setup in **Fig.** 3.1 is thermal crosstalk between them. As the one etalon heats up, thermal radiation causes the other etalon to heat up as well, which causes the proportional-integral-derivative (PID) controller to reduce the output voltage to the heating resistors, causing the etalon to cool. This reduces the thermal radiation absorbed by the first etalon, causing the PID controller to increase the output voltage to the heating resistors. This interaction causes fluctuations in transmission of light through the etalon, or rather, oscillations in the counts detected. This could result in artificial coincidence counts between the two detectors that correspond to thermal crosstalk.

Placing the etalons at opposite ends of the setup, or the use of thermal insulation, are possible measures that can reduce these effects.

In section 2.2.3, we tune the temperature of the etalon to locate the spectrum peaks of the laser diode light. The issue would then be locating the same peak for each etalon before taking correlation measurements. One possible solution would to have the light pass through a common temperature-controlled etalon before the pinhole, and using another temperature-controlled etalon with a lower thickness, each for the transmitted and reflected arm. The first etalon is used to select a peak of the spectrum, while the thinner etalon on each arm (with a larger free spectral range) is used to "filter" the correct peak.

Locating zero baseline

As the 1 mm iris selects a spatial section of the light's output, it can be a challenge to determine which section of the light's spatial profile each iris is selecting, which affects measurements of $g^{(2)}(b, \tau = 0)$. This would lead to wrong angular diameter measurements, measurements lesser than the actual angular diameter for a circular light source. Using the X-Y translation stage that the iris is attached to, we are able to vary the direction along one or two axis, but unable to ensure that both the irises are looking at the same spatial profile (for $b = 0$) or different spatial profiles (for $b > 0$) after passing through the beam splitter. While we can collect measurements outside of the first minima of $g^{(2)}(b)$ and do a fit to translate our data points to coincide with a maximum value of $g^{(2)}(b)$ when $b = 0$, this only gives us the correct offset in one direction. The same measurements in the orthogonal direction must also be carried out to obtain the central spot of the light's spatial profile.

Spatial Profile after Fibres

In the setup for spatial correlation measurements, we chose to use a multimode fibre (MMF) due to the ease of collecting light from the laser diode and having a collimated beam aimed at the pinhole for approximately uniform intensity distribution [22], which is one of the requirements for van-Cittert Zernike Theorem [4, 5]. However, the spatial coherence properties at the output of a MMF is affected by the modal dispersion, fibre length and bandwidth of the light source [23]. Studies on how fibre lengths impacts coherence properties, based on how the intensity patterns change with propagation along the fibre [24, 25], brings about additional ambiguity in the spatial coherence properties at the output end of the MMF. By van-Cittert Zernike Theorem, we require a spatially incoherent source. A spatially coherent output after the MMF would cause the theorem to fail.

In order to remove these extra parameters, we could choose to do without fibres, but whether the light from the laser diode is spatially incoherent to begin with is another question to be answered. There is, however, some means of introducing spatial incoherence through the use of large core diameter step-index polymer optical fibres [26] that can be explored.

Chapter 4

Conclusion

In this thesis, we described the use of light that has bunching properties for both temporal and spatial intensity interferometry. Temporal intensity interferometry, made possible with advancements in detector technologies, allows for spectral analysis through a Fourier transform according to Wiener-Khintchine Theorem [2, 3]. Spatial intensity interferometry, pioneered by Robert Hanbury Brown and Richard Quintin Twiss in 1954, allows for spatial intensity analysis through van-Cittert Zernike Theorem [4, 5].

Through determining of the laser threshold via the power-current curve and spectral full-width half maximum, we ran a semiconductor laser diode below the threshold, and showed that with spectral filtering, the coherence time increases till the bunching signature can be resolved by a 1.2 ns timing resolution avalanche photodiode.

Proceeding with spatial intensity interferometry, we created a setup that could potentially measure $g^{(2)}(b)$, but encountered setbacks that halted progress. We list a few possible challenges that would be encountered in the future and some possible ideas.

As a next step, we could increase the coupling efficiency of divergent light into the single mode fibre with a lens with a wider clear aperture and incorporate translation stages in the z-direction for increased coupling into the fibre. We should also verify that the light incident on the 150 μm pinhole is a spatially incoherent source through possible methods such as a Mach-Zehnder interferometer [27], or employ techniques to create spatial incoherence, such as step-index polymer optical fibres [26], optical coherence tomography [28] or microsphere suspension [14]. We could also experiment with other aperture types, such as slit, double slits and shaped apertures such as square apertures.

References

[1] L. Rayleigh, "XXXI. Investigations In Optics, With Special Reference To The Spectroscope," *The London, Edinburgh, and Dublin Philosophical Magazine and Journal of Science*, vol. 8, no. 49, pp. 261–274, 1879.

[2] N. Wiener, "Generalized Harmonic Analysis," *Acta Mathematica*, vol. 55, pp. 117–258, 1930.

[3] A. Khintchine, "Korrelationstheorie der stationären stochastischen Prozesse," *Math. Ann.*, vol. 109, pp. 604—615, 1934.

[4] F. Zernike, "The Concept Of Degree Of Coherence And Its Application To Optical Problems," *Physica*, vol. 5, no. 8, pp. 785–795, 1938.

[5] P. H. van Cittert, "The Probable Vibration Distribution In A Plane Illuminated By A Light Source Directly Or By A Lens," *Physica*, vol. 1, pp. 201–210, 1934.

[6] M. M. Colavita, M. Shao, and D. H. Staelin, "Atmospheric Phase Measurements With The Mark Iii Stellar Interferometer," *Applied Optics*, vol. 26, no. 19, pp. 4106–4112, 1987.

[7] R. H. Brown and R. Q. Twiss, "A New Type of Interferometer for Use in Radio Astronomy," *Philos. Mag.*, vol. 45, no. 366, pp. 663–682, 1954.

[8] A. L. R. R. H. Brown and F. Davis, "The Angular Diameter of 32 stars," *MNRAS*, vol. 167, pp. 121–136, 1974.

[9] W. Martienssen and E. Spiller, "Coherence and Fluctuations in Light Beams," *American Journal of Physics*, vol. 32, pp. 919–926, 1964.

[10] M. Fox, *Quantum Optics: An Introduction*, vol. 15. OUP Oxford, 2006.

[11] A. J. F. Siegert, *On The Fluctuations In Signals Returned By Many Independently Moving Scatterers*. Radiation Laboratory, Massachusetts Institute of Technology, 1943.

[12] T. P. K. et al., "Measuring temporal photon bunching in blackbody radiation," *The Astrophysical Journal Letters*, vol. 789, no. 1, p. L10, 2014.

[13] T. Asakura, "Spatial coherence of laser light passed through rotating ground glass," *Opto-electronics*, vol. 2, pp. 115–123, 1970.

[14] D. Dravins, T. Lagadec, and P. D. Nunez, “Optical aperture synthesis with electronically connected telescopes,” *Nature communications*, vol. 6, no. 1, pp. 1–5, 2015.

[15] R. Loudon, *The Quantum Theory of Light*. Clarendon Press, 1973.

[16] D. B. Scarl, “Measurements of photon correlations in partially coherent light,” *Physical Review*, vol. 175, no. 5, p. 1661, 1968.

[17] C. Kurtsiefer, P. Zarda, S. Mayer, and H. Weinfurter, “The Breakdown Flash Of Silicon Avalanche Photodiodes-back Door For Eavesdropper Attacks?,” *Journal of Modern Optics*, vol. 48, no. 13, pp. 2039–2047, 2001.

[18] D. G. Peterson and A. Yariv, “Interferometry and Laser Control with Solid Fabry–Perot Etalons,” *Applied Optics*, vol. 5, no. 6, pp. 985–991, 1966.

[19] W. R. Leeb, “Losses Introduced By Tilting Intracavity Etalons,” *Applied physics*, vol. 6, no. 2, pp. 267–272, 1975.

[20] J. M. Green, “The ’ Walk-off’ Effect In Fabry-perot Etalons-limitations To ’ Single-shot’ Linewidth Measurements At Longer Wavelengths,” *Journal of Physics E: Scientific Instruments*, vol. 13, no. 12, pp. 1302–1304, 1980.

[21] W. Sellmeier, “Ueber die durch die Aetherschwingungen erregten Mitschwingungen der Körpertheilchen und deren Rückwirkung auf die ersteren, besonders zur Erklärung der Dispersion und ihrer Anomalien,” *Annalen der Physik und Chemie*, vol. 223, no. 11, pp. 386—-403, 1872.

[22] D. Véron, H. Ayral, C. Gouedard, D. Husson, J. Lauriou, O. Martin, B. Meyer, M. Rostaing, and C. Sauteret, “Optical Spatial Smoothing Of Nd-glass Laser Beam,” *Optics communications*, vol. 65, no. 1, pp. 42–46, 1988.

[23] E. G. Rawson, J. W. Goodman, and R. E. Norton, “Frequency Dependence Of Modal Noise In Multimode Optical Fibers,” *JOSA*, vol. 70, no. 8, pp. 968–976, 1980.

[24] B. Crosignani and P. Di Porto, “Coherence of an electromagnetic field propagating in a weakly guiding fiber,” *Journal of Applied Physics*, vol. 44, no. 10, pp. 4616–4617, 1973.

[25] B. Crosignani, B. Daino, and P. Di Porto, “Interference Of Mode Patterns In Optical Fibers,” *Optics Communications*, vol. 11, no. 2, pp. 178–179, 1974.

[26] M. A. Illarramendi, R. Hueso, J. Zubia, G. Aldabaldetreku, G. Durana, and A. Sánchez-Lavega, “A Daylight Experiment For Teaching Stellar Interferometry,” *American Journal of Physics*, vol. 82, no. 7, pp. 649–653, 2014.

[27] A. Efimov, “Spatial Coherence At The Output Of Multimode Optical Fibers,” *Optics express*, vol. 22, no. 13, pp. 15577–15588, 2014.

[28] A.-H. Dhalla, J. V. Migacz, and J. A. Izatt, “Crosstalk Rejection In Parallel Optical Coherence Tomography Using Spatially Incoherent Illumination With Partially Coherent Sources,” *Optics letters*, vol. 35, no. 13, pp. 2305–2307, 2010.

Appendix A

Experimental Plots and Photos

Spectrum Plots with Gaussian Fits

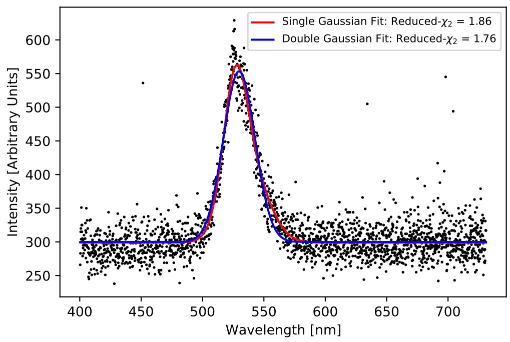

(a) Spectrum with fits for input current 5 mA

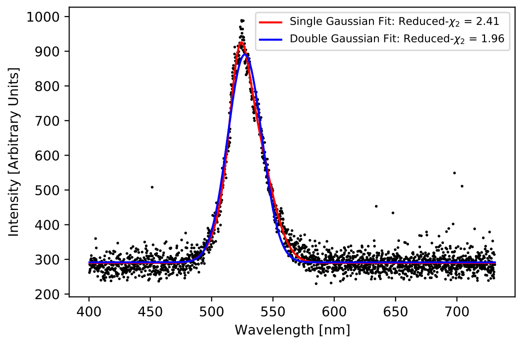

(b) Spectrum with fits for input current 15 mA

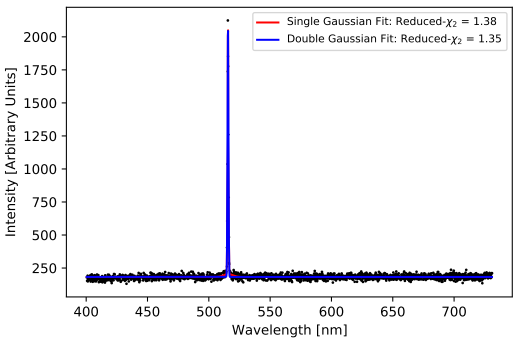

(c) Spectrum with fits for input current 35 mA

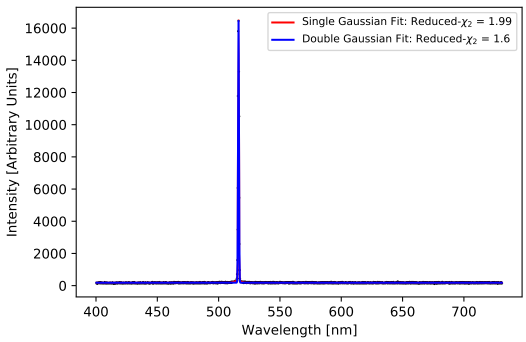

(d) Spectrum with fits for input current 45 mA

Fig. A.1 Single and double Gaussian fits for spectrum data at varying input currents. Measurements taken by OceanOptics spectrometer.

Photos of Setup

Setup for temporal second order correlation measurements:

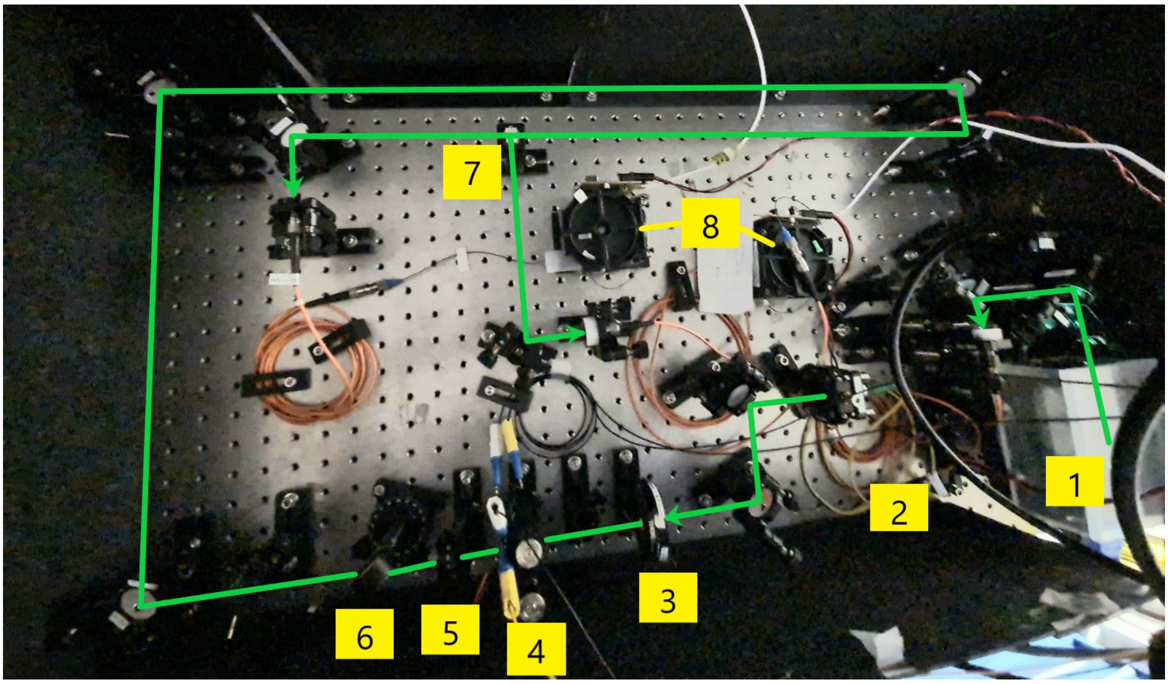

Fig. A.2 Green lines indicate path of light. The laser diode (1) is coupled into a multimode fibre that is mated to a single mode fibre (2). Light is then incident on a half-wave plate (3) and a 1 mm thick etalon. Transmitted light then passes through a linear polariser (5) and a bandpass filter (6) before it is incident on a polarising beamsplitter (7), with light from each arm coupled into a multimode fibre that is connected to passively quenched avalanche photodiodes (8). They are electronically connected to a timestamp unit (not shown). Orange fibres are multimode fibres while yellow fibres are single mode fibres.

Setup for spatial second order correlation measurements:

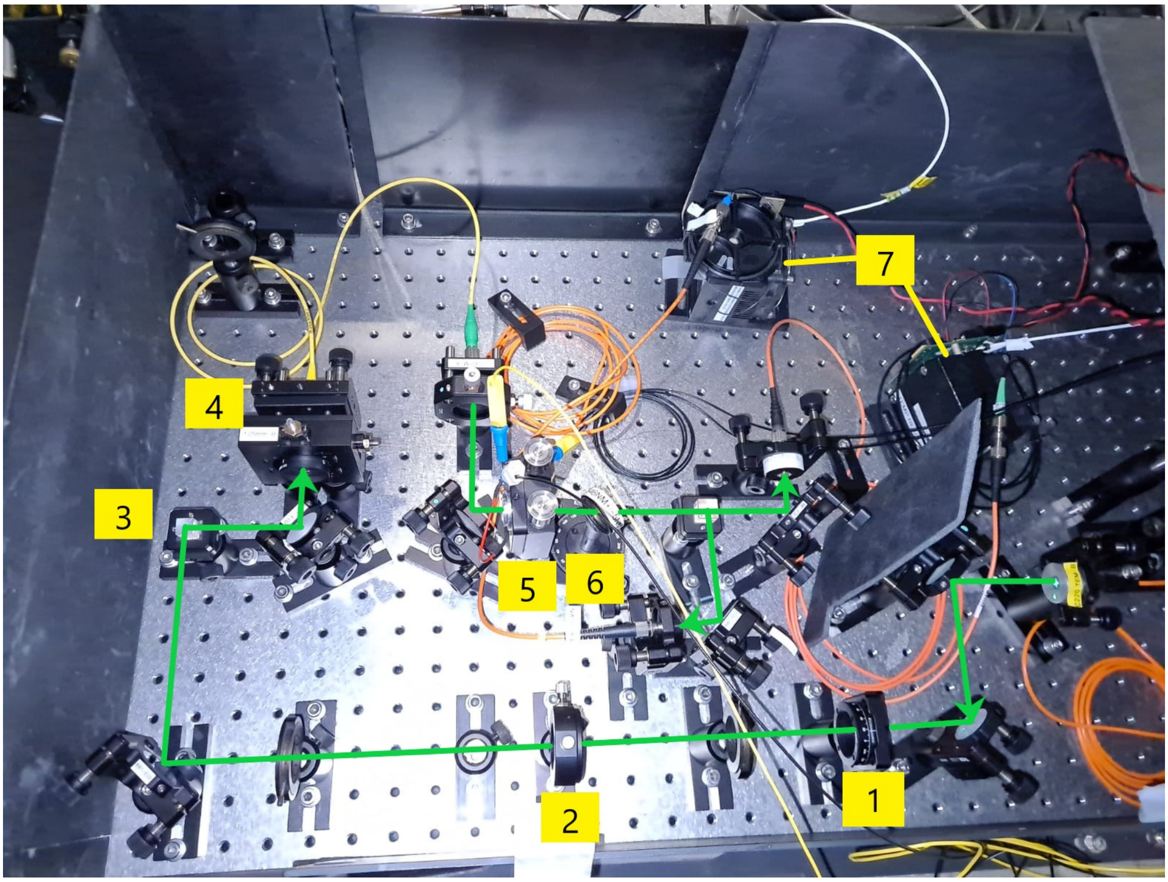

Fig. A.3 Green lines indicate path of light. After light from the laser diode has passed through a multimode fibre and is collimated with an aspheric lens, it is incident on a film linear polariser (1) before it hits the 150 μm pinhole (2). It is then incident on a non-polarising beamsplitter (3). We first setup the reflected arm, which consists of a variable iris (minimum aperture size of 1 mm) on a X-Y translation stage, with an aspheric lens held by a tip-tilt stage in a cage system (4). After passing through the single mode fibre, it is then incident on the 1 mm etalon (5) before passing through a optical bandpass filter (6). Another non-polarising beam splitter directs light into two separate aspherics and connected to two detectors (7) with multimode fibres. They are then electronically connected to a timestamp unit (not shown) via NIM cables (white cables).

Miscellaneous

(a) Timestamp unit used for coincidence measurements. Channels 1 and 2 were used, with an electronic delay introduced to channel 2. The dead time of the timestamp unit is 2 ns.

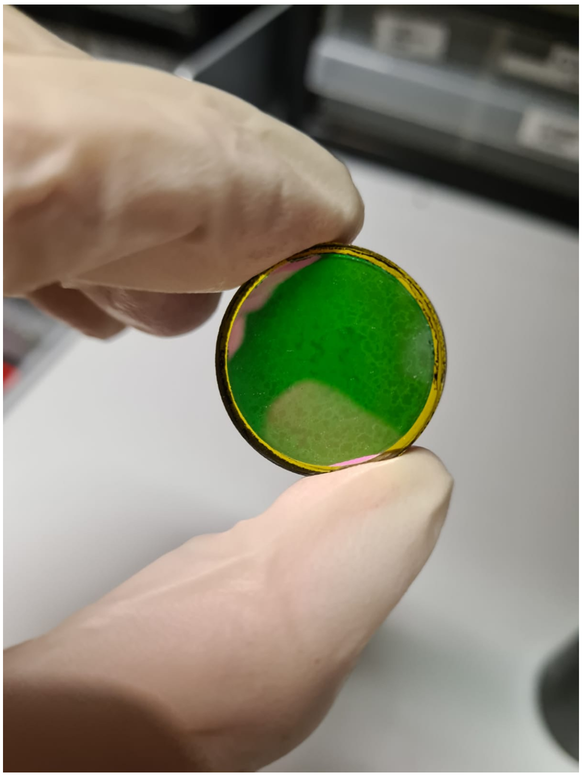

(b) Optical bandpass filter used, with centre wavelength of 546 nm and about 8 nm FWHM.

Appendix B

Tuning Rate of Etalon

Coefficients	Values
B_1	$4.73115591 \cdot 10^{-1}$
B_2	$6.31038719 \cdot 10^{-1}$
B_3	$9.06404498 \cdot 10^{-1}$
C_1	$1.29957170 \cdot 10^{-2}$
C_2	$4.12809220 \cdot 10^{-3}$
C_3	$9.87685322 \cdot 10^{1}$

Table B.1 Empirical Sellmeier coefficients for wavelength-dependent Sellmeier equation.

Coefficients	Values
D_0	$2.18 \cdot 10^{-5}$
D_1	$2.45 \cdot 10^{-8}$
D_2	$-2.72 \cdot 10^{-11}$
E_0	$2.31 \cdot 10^{-7}$
E_1	$2.21 \cdot 10^{-10}$
λ_{TK}	235nm

Table B.2 Empirical Sellmeier coefficients for wavelength-temperature-dependent Sellmeier equation.

From the definition of free spectral range defined in equation (2.10), we can differentiate it with respect to temperature T:

$$\frac{\partial FSR}{\partial T} = -\frac{c}{2n(\lambda,T)L}\left(\frac{1}{n(\lambda,T)}\frac{\partial n(\lambda,T)}{\partial T} + \frac{1}{L}\frac{\partial L}{\partial T}\right), \tag{B.1}$$

where we can obtain the $\frac{\partial n(\lambda,T)}{\partial T}$ term from the Sellmeier coefficients in Table B.2. Substituting the values into the wavelength-temperature-dependent Sellmeier equation:

$$\begin{aligned}\frac{\partial n(\lambda,T)}{\partial T} &= \frac{n^2(\lambda,T)-1}{2\cdot n(\lambda,T)}\left(D_0\cdot\Delta T + D_1\cdot\Delta T^2 + D_2\cdot\Delta T^3 + \frac{E_0\cdot\Delta T + E_1\cdot\Delta T^2}{\lambda^2-\lambda_{TK}^2}\right)\\ &\approx 8.92\cdot 10^{-6}K^{-1}\end{aligned}$$

We also obtain the refractive index of the etalon substrate (Suprasil 311) at 515 nm using the equation in (2.11) and substituting values in Table (B.1) to obtain a value of about 1.4615.

Along with a thermal expansion coefficient of $5.1\cdot 10^{-7}K^{-1}$, we substitute these values into equation (B.1), we obtain for a 1 mm thick etalon made of Suprasil 311:

$$\begin{aligned}\frac{\partial FSR}{\partial T} &= -\frac{c}{2(1.4615)(0.001)}\left(\frac{1}{1.4615}(8.92\cdot 10^{-6}) + 5.1\cdot 10^{-7}\right)\\ &= -0.678\,MHz/K\end{aligned}$$

The mode number m that corresponds to 515 nm in the 1 mm etalon is about 5676, hence at the mode corresponding to 515 nm, the tuning rate is calculated to be -3.85 GHz/K. Note that this value is just an estimate of the actual tuning rate of the etalon.